Journal of Hydrology: Regional Studies 64 (2026) 103303

Contents lists available at ScienceDirect

Journal of Hydrology: Regional Studies

journal homepage: www.elsevier.com/locate/ejrh

A modeling framework for disentangling the impacts of changing climate and land uses on terrestrial water-carbon balance under SSP-RCP scenarios

Xiaola Wang [a,1], Jiangchao Qiu [c,1], Kai Duan [b,*], Ge Sun [d], Jianhua Wang [a], Huan Liu [a], Xuanxuan Wang [a], Peng Hu [a,*]

[a] *State Key Laboratory of Water Cycle and Water Security, China Institute of Water Resources and Hydropower Research, Beijing 100038, PR China*
[b] *School of Civil Engineering, Sun Yat-Sen University, Zhuhai 519082, PR China*
[c] *Department of Earth, Atmospheric, and Planetary Sciences, Massachusetts Institute of Technology, Cambridge, MA 02139, USA*
[d] *Eastern Forest Environmental Threat Assessment Center, Southern Research Station, USDA Forest Service, Research Triangle Park, NC 27709, USA*

ARTICLE INFO

Keywords:
Attribution
Climate change
Land use change
Pearl River Basin
Watershed water-carbon cycles

ABSTRACT

Study region: The Pearl River Basin (PRB) in South China
Study focus: Understanding impacts of climate and land use changes on terrestrial water-carbon balance is critical for sustainable water-land management and climate change adaptation. Yet attributing responses to individual drivers remains challenging. We develop an integrated modeling framework to quantify contributions of changes in climate and land use and their offsetting effects on key ecohydrological fluxes.
New hydrological insights for the region: In the PRB, we evaluate water and carbon flux responses to climate (precipitation, potential evapotranspiration (*PET*)) and land use patterns (e.g., forest and urban) across SSP-RCP scenarios (SSP126, SSP370, SSP585) in the near future (NF, 2021–2050) and far future (FF, 2071–2100). Climate drivers generally exert stronger impacts on water and carbon fluxes than land use drivers across the PRB, whereas land use impacts are non-negligible and spatially heterogeneous. Specifically, urbanization increases runoff (*R*) (up to 34% under NF-SSP585) and reduces net ecosystem productivity (*NEP*) (up to −8% under FF-SSP585), most pronounced in the Pearl River Delta. In contrast, forest expansion reduces *R* and enhances carbon sequestration especially in Dongjiang River Basin. *PET* impacts on regional carbon sinks are highly scenario-dependent: higher *PET* enhances carbon fluxes via increased actual evapotranspiration in the NF, whereas under FF-SSP370 and FF-SSP585, persistently elevated *PET* induces hot-dry stress that outweighs positive drivers and suppresses *NEP*.

1. Introduction

Water and carbon cycles are intrinsically linked and play a pivotal role in controlling material and energy exchanges between the terrestrial ecosystems and the atmosphere (Gentine et al., 2019; Wang et al., 2024). Soil moisture (*SM*) and actual evapotranspiration (*ETa*) are the key factors influencing plant photosynthesis, while vegetation, through canopy interception and transpiration, feeds back

* Correspondence to: School of Civil Engineering, Sun Yat-Sen University, Tangjiawan Town, Xiangzhou District, Zhuhai 519082, PR China.
E-mail addresses: duank6@mail.sysu.edu.cn (K. Duan), hp5426@126.com (P. Hu).
[1] These authors contributed equally to this work: Xiaola Wang, Jiangchao Qiu

https://doi.org/10.1016/j.ejrh.2026.103303
Received 1 December 2025; Received in revised form 15 February 2026; Accepted 25 February 2026
Available online 3 March 2026

into the hydrological system (Kannenberg et al., 2024; Li et al., 2024; Sun et al., 2025; Vereecken et al., 2022). As carbon sequestration is heavily reliant on water from soil and air, this creates inherent conflicts between water yield and carbon sequestration in watersheds (Jackson et al., 2005; Sun et al., 2025). Understanding water-carbon response to the changing environment is essential for the integrated management of water and land resources, securing water supply, and achieving carbon neutrality (IPCC, 2023; Quan et al., 2019; Zhang et al., 2025).

The impacts of environmental changes on water and carbon cycles are multifaceted and intricate, with climate and land use/cover change identified as two primary drivers (Dale et al., 1997; Hou et al., 2025; Huang et al., 2015; Pilla et al., 2022; te Wierik et al., 2021; Sitch et al., 2024; Yang et al., 2025). Climate change refers to long-term changes in temperature (*T*), precipitation (*PRE*), and other weather patterns, largely driven by anthropogenic greenhouse-gas emissions (IPCC, 2013; Rawat et al., 2024). These changes profoundly alter key terrestrial hydrological variables (e.g., *ETa*, runoff (*R*), and *SM*) and the carbon sequestration capacity of ecosystems. For example, rising temperature and changing *PRE* can reduce water yield but increase gross ecosystem productivity (*GEP*) by shifting water partitioning toward evapotranspiration (Duan et al., 2016). Similarly, land use change caused by urbanization, deforestation, reclamation, or afforestation modifies surface energy and water partitioning and can influence local *PRE*, thereby reshaping ecohydrological processes and terrestrial carbon balance (Arantes et al., 2016; Teuling et al., 2019; te Wierik et al., 2021; Zhao et al., 2022). Extensive evidence shows that afforestation enhances ecosystem carbon sequestration while increasing water consumption, lowering soil water availability, and reducing watershed water yield (Farley et al., 2005; Du et al., 2021; Zhang et al., 2021; Zhao et al., 2022). In contrast, rapid urbanization expands impervious surfaces, which reduces infiltration and flood storage and diminishes land carbon storage (Seto et al., 2012; Li et al., 2020; Wu et al., 2024).

Numerous studies have sought to diagnose the characteristics and causes of watershed water and carbon cycles and to quantify the contributions of individual drivers to changes in water and carbon fluxes. These studies have widely applied four approaches, including paired catchment comparisons, empirical statistical analyses, the elasticity method, and ecohydrological modeling (Duan et al., 2021; Luan et al., 2021). The paired catchment approach relies on observational quality and subjective assessments of watershed similarity, which constrains its transferability to medium and large watersheds (Bosch and Hewlett, 1982; Kang and Sharma, 2024; Lørup et al., 1998). Empirical statistical methods are computationally simple but lack basic physics and require substantial measurements (Xiao et al., 2022; Xiao et al., 2023; Wu et al., 2017). The elasticity method has been widely used in recent years, particularly the Budyko-based elasticity method, which neglects changes in water storage and is therefore best suited to multi-year or annual scales (Budyko and Miller, 1974; Gan et al., 2021; Chang et al., 2024). In contrast, ecohydrological models enable controlled simulations with explicit physics, allowing attribution in ungauged areas and flexible projections under future conditions. For instance, Li et al. (2020) coupled Water Supply Stress Index (WaSSI) with regression and causal analyses across the conterminous United States and showed that urbanization lowers *GEP* via vegetation loss and impervious surfaces, yielding a clear trade-off between higher water yield and lower carbon uptake. Similarly, in Mediterranean mountain croplands, Khorchani et al. (2022) used regional Hydro-Ecological Simulation System (RHESSys) to demonstrate that afforestation raises net ecosystem productivity (*NEP*) yet reduces runoff through enhanced transpiration, whereas warming alone had little impact. Extending this attribution capability to quantify driver importance, Hutley et al. (2022) combined Tethys-Chloris with random forest analysis in Australian savannas and found that rising CO_2, *PRE*, and air temperature jointly explain approximately 90% of *GEP* trends, with wet-season fluxes limited by radiation and dry-season fluxes constrained by *SM*. Existing studies have acknowledged the distinct impacts of climate change and land use change on regional water and carbon cycles. However, many studies still treat water and carbon fluxes in isolation, with insufficient attention to their coupled responses within a unified framework. Moreover, climate change and anthropogenic activities are frequently simplified into broad driver categories, and there is a lack of systematic analyses across diverse scenarios and spatial scales to disentangle the individual offsetting or synergistic effects of different hydroclimatic and socioeconomic drivers. Furthermore, water-carbon feedbacks specifically triggered by conversions between different land-use classes have yet to be quantitatively characterized.

To tackle these questions, we develop a quantitative attribution framework based on the WaSSI eco-hydrological model (Caldwell et al., 2012; Duan et al., 2019; Sun et al., 2011) and an improved fixing-changing method (Duan et al., 2017). Specifically, we aim to: 1) project future evolution of water and carbon fluxes across shared socioeconomic pathway-representative concentration pathway (SSP-RCP) scenarios from 2015 to 2100, SSP126, SSP370, and SSP585 are selected as representative scenarios, corresponding to low-emission, medium-emission, and high-emission pathways, respectively; and 2) quantitatively attribute future changes in water availability and ecosystem productivity to climate drivers (*PRE*, *PET*) and land use drivers (cropland (*CRO*), forest (*FOR*), grassland (*GRA*), urban (*URB*), water (*WAT*), and barren (*BAR*)) across scenarios in both near future (NF: 2021–2050) and far future (FF: 2071–2100). The Pearl River Basin (PRB) is a typical humid region in southern China, characterized by abundant precipitation, high evapotranspiration, and dense subtropical vegetation. As a vital carbon sink and water-conservation area, it plays a crucial role in China's coupled water-carbon cycling while supporting rapid socioeconomic development. Consequently, understanding how future climate and land use changes impact water-carbon trade-offs in the PRB is critical for guiding ecological restoration and land use management.

2. Study area and datasets

2.1. The Pearl River Basin

The Pearl River is the largest river in southern China. Its basin covers approximately 454,000 km^2 in total, of which about 442,000 km^2 lie within China, and it comprises four major sub-regions, namely the Pearl River Delta (PRD), Dongjiang (DJRB), Beijiang (BJRB), and Xijiang (XJRB) River Basins (Qiu et al., 2022). Topography slopes from the northwestern highlands toward the southeastern lowlands. The region experiences a tropical to subtropical climate, with of 14–22 °C and mean annual *PRE* of 1200–2200 mm. The rainy season spans April to September and contributes approximately 70–85% of annual *PRE* (Yan et al., 2015). Based on 2010 MODIS land use, the dominant classes are grassland (41.7%), shrubland (29.2%), cropland (11.8%), and evergreen forest (11.3%).

2.2. Datasets

2.2.1. Historical data

The historical datasets used in this study included sub-basin attributes, soil properties, impervious surface area, leaf area index (*LAI*), land use, and climate forcing. Specifically, sub-basin attributes were derived from HydroSHEDS, including DEM, sub-basin boundaries, and river networks. Historical land use was obtained from the MODIS MCD12Q1 product under the IGBP classification, with two snapshots from 2010 and 2015 used in this study. Historical climate forcing was taken from the China Meteorological Forcing Dataset (CMFD) for the baseline period (1985–2014), including air temperature, atmospheric pressure, specific humidity, wind speed, downward shortwave radiation, and *PRE*. Additional details on spatial resolution, units, and projections are listed in Table 1 to ensure consistency across inputs. Given that the WaSSI-PRB model was previously calibrated and validated in Wang et al. (2022) (briefly summarized in Section 3.3), the historical data described here do not include the complete set used for WaSSI-PRB model development and validation (e.g., longer historical CMFD forcing, in-situ runoff observations, and remote-sensing products for *ETa* and *GEP*).

2.2.2. Future scenarios

We used bias-corrected and downscaled outputs from five global climate models (GCMs) participating in ISIMIP3b (Lange, 2021) to drive future climate scenarios, and details of the selected GCMs are listed in Table S1. ISIMIP3b provides climate forcing at 0.5° × 0.5° for 2015–2100 under SSP126, SSP370, and SSP585, including *PRE*, air temperature (mean, maximum and minimum), wind speed, downward shortwave radiation, and relative humidity.

The future land use change data utilized in this study were derived from Liao et al. (2020), which provided land use projections for China at 5-year intervals and a spatial resolution of 5 km under eight SSP-RCP scenarios for the period 2015–2100. The dataset was developed by extracting land use demand trajectories from the Land-Use Harmonization version 2 (LUH2) dataset, calibrating the 2015 land use from LUH2-China using historical MODIS observations, and simulating future changes in six land use classes (forest, grassland, cropland, urban, barren, and water) using the FLUS model. Consequently, the original 2015 LUH2-China land use data were replaced with the MODIS MCD12Q1 map.

3. Methodology

3.1. Overall framework

The framework for quantifying the impacts of climate and land use changes on terrestrial water and carbon cycles under SSP-RCP scenarios comprises three steps (Fig. 2). The first step involves hydroclimatic drivers' spatiotemporal interpolation and land use reclassification. Gridded datasets at various resolutions were transformed to a unified sub-basin and monthly scale to provide accurate and consistent inputs for subsequent modeling. The second step is vegetation-specific water-carbon modeling. Utilizing future climate and land use data, we employed an enhanced WaSSI model (WaSSI-PRB, as described in Section 3.3) to simulate the combined impacts of climate and land use changes on sub-basin water and carbon fluxes (e.g., *ETa*, *R*, *SM*, *GEP*, *NEP* and *RE* (ecosystem respiration)*)* under SSP126, SSP370, and SSP585. The third step is the quantitative attribution of water-carbon balance. We coupled the WaSSI-PRB with a fixing-and-changing method to estimate the contributions of individual climate and land use drivers to water and carbon fluxes in NF (2021–2050) and FF (2071–2100). Additionally, the spatial distribution characteristics of the dominant factors affecting water and carbon fluxes at the sub-basin scale are analyzed.

Table 1
Summary of the datasets used in this study.

Data	Time period	Spatial resolution	Temporal resolution	Source
Sub-basin attributes	2008	90 m	—	Lehner et al. (2008)
Soil properties	–	1 km	—	Shi et al. (2010)
Impervious cover area	2010	30 m	—	Brown de Colstoun et al. (2017)
Leaf area index	2000–2016	1 km	8-day	Yuan et al. (2011)
Historical Land use data	2010, 2015	500 m	—	Friedl and Sulla-Menashe, (2019)
Historical climate data	1985–2014	0.1°	3-h	Yang et al. (2010); Yang et al. (2020); He et al. (2020)
Future climate data	2015–2100	0.5°	1-day	Lange (2021)
Future land use data	2015–2100	5 km	5-year	Liao et al. (2020)

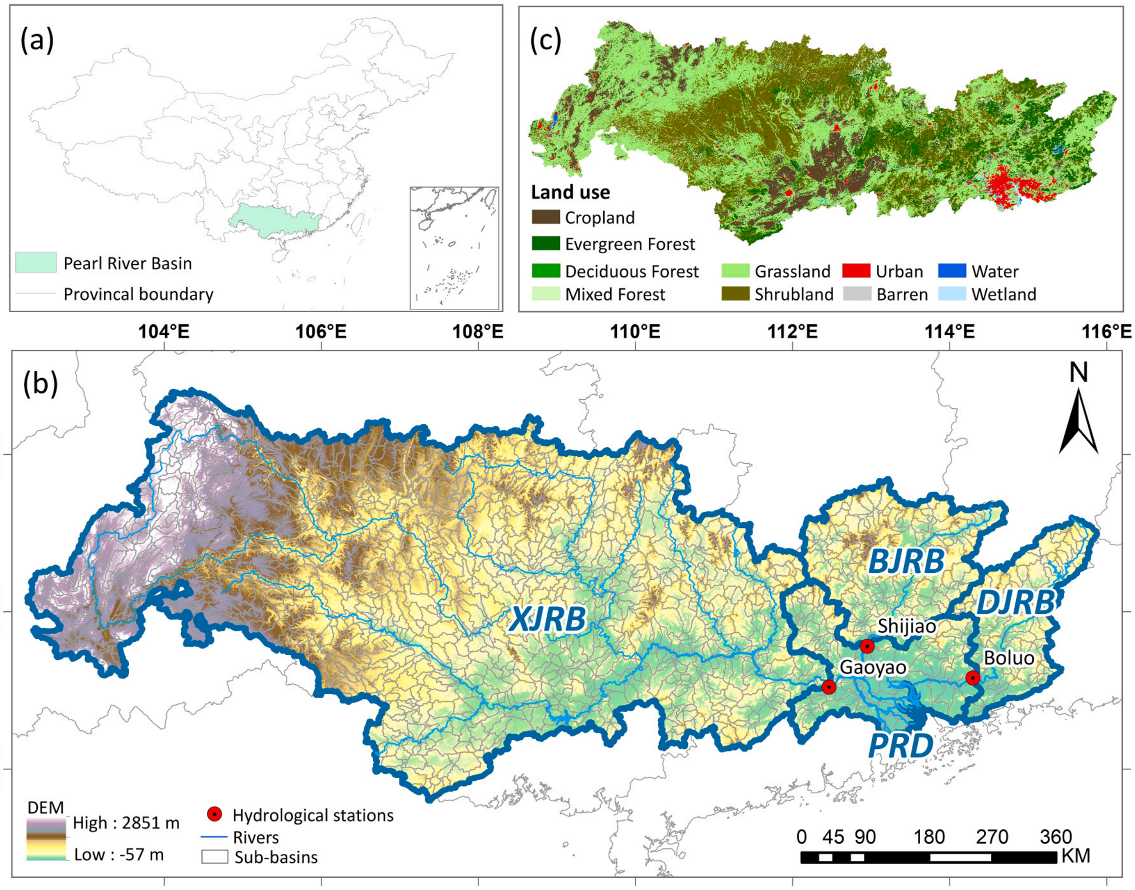

Fig. 1. Location (a), topography (b), and land use (c) of the Pearl River Basin (PRB). PRD, DJRB, BJRB, and XJRB indicate the Pearl River Delta, Dongjiang, Beijiang, and Xijiang River Basins, respectively.

3.2. Input data preprocessing

Data preprocessing includes hydroclimatic drivers' spatiotemporal interpolation and land use reclassification. We firstly partitioned the PRB into 1675 sub-basins to drive WaSSI-PRB, following the Level-9 subdivision of HydroSHEDS. The PRD, DJRB, BJRB, and XJRB contain 111, 101, 150, and 1313 sub-basins, accounting for approximately 7%, 6%, 9%, and 78% of the basin area. To ensure spatiotemporal consistency, all gridded datasets were harmonized to a common sub-basin-monthly scale. Non-monthly products (e.g., 3-hourly and 8-day datasets) were temporally aggregated into monthly values through summation or averaging, depending on their physical attributes. For spatial processing, high-resolution continuous variables were converted to sub-basin values using area-weighted averaging. For categorical data such as land-use types, the fractional area of each class was quantified within each sub-basin boundary to determine the corresponding *LAI* and impervious surface fractions. Coarser-resolution datasets were transferred to the sub-basin scale using a spatial interpolation based on the Thiessen-polygon method, following the protocol documented in Duan et al. (2022). Further preprocessing details are available in the WaSSI User Guide (Caldwell et al., 2019).

In addition, land use datasets required harmonization and reclassification across products and scenarios. For land use, we harmonized the FLUS and MODIS classification systems to the WaSSI scheme for model inputs. A conversion matrix between FLUS and MODIS was adopted from Liao et al. (2020). First, the 2015 MODIS map was used to compute sub-basin fractions for each land use class. Second, FLUS projections (six classes) were reclassified to the MODIS system (16 classes) using those fractions. Finally, MODIS classes were aggregated to ten categories following the Anderson primary scheme: cropland, evergreen forest, deciduous forest, mixed forest, shrubland, grassland, urban, water, wetland, and barren (Konarska et al., 2002).

3.3. Vegetation-specific water-carbon modeling

The WaSSI model is an integrated, water-centric monthly model with three core modules: evapotranspiration, water cycling, and carbon cycling (Sun et al., 2011). It has been used to assess the impacts of climate change, land use change, and water demand on basin hydrology and ecosystem function, and has seen wide application in the United States (Caldwell et al., 2012; Duarte et al., 2024), China (Tang et al., 2018), Australia (Liu et al., 2018) and Rwanda (Bagstad et al., 2018).

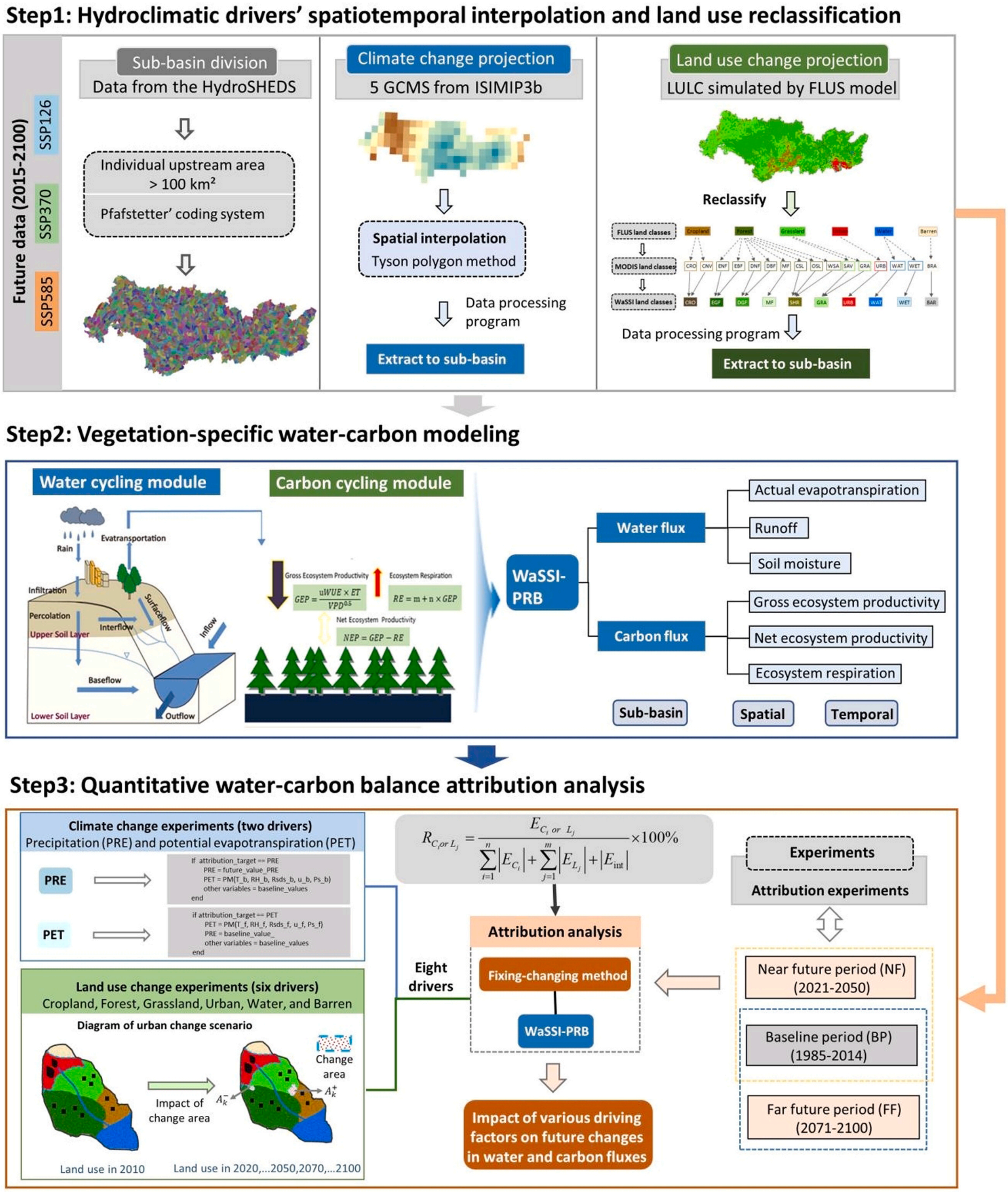

Fig. 2. The overall framework summarizing three parts of this study.

The WaSSI model consists of water and carbon cycling modules, and is driven by sub-basin attributes, impervious surface area, *LAI*, land use, and climate forcing. In this study, the modules are used to simulate water fluxes (*R*, *ETa*, and *SM*) and carbon fluxes (*GEP*, *RE*, and *NEP*) for each land use class at the sub-basin scale across the PRB. In the water cycling module, potential actual evapotranspiration (*PAET*) is first derived from an empirical relationship among *PET*, *LAI*, and *PRE* , and it represents evaporative demand without soil moisture constraints. The Sacramento Soil Moisture Accounting Model (SAC-SMA) model is then used to impose a supply constraint so that *ETa* reflects the available water in layered soil reservoirs, while infiltration, soil moisture storage, and drainage are also simulated by SAC-SMA. In the carbon cycling module, *GEP* is estimated from an empirical relationship between *ETa* and biome-specific *WUE*, and then *RE* is inferred from *GEP* using an empirical formula, thereby yielding *NEP*. More details on the WaSSI model are available in Sun et al. (2011) and Caldwell et al. (2012).

We developed an enhanced version of WaSSI (WaSSI-PRB), in which the water and carbon cycling module were improved to account for regional characteristics and climate variability. In the water cycling module, the (Food and Agriculture Organization of the United Nations) FAO Penman-Monteith (PM) reference evapotranspiration equation (Allen et al., 1998) replaced the original Hamon equation (Hamon, 1963) to compute *PET*, providing a more comprehensive representation of the combined effects of radiation, humidity, wind speed, and other climate drivers on the *ET* process. To improve regional applicability and simulation accuracy, we applied the SCE-UA algorithm (Duan et al., 1994) to calibrate four key parameters in the *PAET* equation. Calibration was conducted separately for sub-regions (PRD, DJRB, BJRB, and XJRB) using observed monthly runoff data, and the specific equations are given below:

$$\mathrm{PAET_{XJRB}} = 0.1740 \times \mathrm{PRE} + 0.5020 \times \mathrm{PET} + 5.3100 \times \mathrm{LAI} + 0.0222 \times \mathrm{PET} \times \mathrm{LAI} \tag{1}$$

$$\mathrm{PAET_{BJRB}} = 0.2498 \times \mathrm{PRE} + 0.0011 \times \mathrm{PET} + 7.5789 \times \mathrm{LAI} + 0.0010 \times \mathrm{PET} \times \mathrm{LAI} \tag{2}$$

$$\mathrm{PAET_{DJRB}} = 0.3010 \times \mathrm{PRE} + 0.3020 \times \mathrm{PET} + 6.4452 \times \mathrm{LAI} + 0.0010 \times \mathrm{PET} \times \mathrm{LAI} \tag{3}$$

where *PRE* is precipitation, *PET* is potential evapotranspiration, and *LAI* is the monthly average leaf area index. The four calibrated parameters are the empirical coefficients on *PRE*, *PET*, *LAI*, and $PET \times LAI$ in Eqs. (1)-(3). For PRD sub-basins, *PAET* coefficients were adopted from the geographically nearest subregion (DJRB, BJRB, or XJRB), given the limited runoff observations within PRD.

In the carbon cycling module, the original WaSSI model estimated *GEP* using a simple linear relationship ($\mathrm{GEP} = \mathrm{WUE} \times \mathrm{ETa}$), without accounting for the nonlinear effects of atmospheric dryness. To address this limitation, we adopted the underlying water use efficiency (*uWUE*) framework proposed by Zhou et al. (2014), which incorporates vapor pressure deficit (*VPD*) to better reflect the coupling between carbon uptake and water loss. In our implementation, *GEP* is calculated as:

$$\mathrm{GEP} = \frac{\mathrm{uWUE} \times \mathrm{ETa}}{\mathrm{VPD}^{0.5}} \tag{4}$$

where *uWUE* is a land use specific constant adopted from Du (2019) based on the FLUXNET2015 dataset and ranges from 0.00 to 2.74 g C $\mathrm{kPa}^{0.5}$ kg^{-1} H_2O (see Supplementary Table S2). *VPD* is computed at the monthly scale using the FAO-56/Tetens formulation, incorporating maximum/minimum temperature (*Tmax* and *Tmin*) and relative humidity framework to minimize bias from the nonlinear temperature dependence of saturation vapor pressure (Allen et al., 1998; Zongxing et al., 2014). Based on the *GEP* estimation, we adopted empirical formulas from the original WaSSI model to calculate *RE* and *NEP*, where *RE* is modeled as a linear function of *GEP*:

$$\mathrm{RE} = m + n \times \mathrm{GEP} \tag{5}$$

$$\mathrm{NEP} = \mathrm{GEP} - \mathrm{RE} \tag{6}$$

where *m* and *n* are empirical coefficients representing base respiration and carbon-use efficiency, respectively (Sun et al., 2011).

It is worth noting that the water cycling module of WaSSI-PRB was calibrated and validated in our previous work (Wang et al., 2022), where the model structure and input datasets were established. The corresponding validation results are shown in Supplementary Section S1 Fig. S1 and Fig. S2. In addition, the carbon cycling module is refined and validated in this study, and details of its results are also described in Supplementary Section S1.

3.4. Quantitative water-carbon balance attribution

We applied an improved fixing-changing method to disentangle the individual and interactive impacts of multiple driving factors, based on simulations from the WaSSI-PRB model (Duan et al., 2017, 2022, 2023). This enhanced approach enables a more combined and quantitative assessment of the relative contributions of each factor to changes in water and carbon fluxes.

Eco-hydrological models are widely used to evaluate the impacts of climate change and human activities on regional water and carbon dynamics. A common approach involves coupling physics-based models with the fixing-changing method to conduct controlled simulations for single-factor attribution (Lu et al., 2015; Woldesenbet et al., 2017; Souza da Silva et al., 2023). However, due to nonlinear interactions among input variables, the traditional fixing-changing method usually fails to capture inter dependencies between factors. This limitation can result in a discrepancy between the sum of individual contributions and the total system impact, a phenomenon referred to as non-closure. To address this issue, we adopted an enhanced fixing-changing method that explicitly incorporates interaction impacts.

The experiments are structured as follows: the baseline period is defined as 1985–2014, while the near future and far future periods are 2021–2050 and 2071–2100, respectively. Within each future period, only one individual climate variable or land use class is varied, while all other variables are held at their baseline values. We run WaSSI-PRB to assess changes in water and carbon fluxes relative to the baseline. The relative contribution of each factor is computed as:

$$\Delta E = f(C^{t_b}, L^{t_f}) - f(C^{t_b}, L^{t_f}) = \sum_{i=1}^{n} E_{C_i} + \sum_{j=1}^{m} E_{L_j} + E_{Int} \tag{7}$$

Here,ΔErepresents the combined impact of simultaneous changes in all climate variables ($C_i, i = 1,2,\ldots,n$) and land use classes ($L_j, j = 1,2,\ldots,m$) on water and carbon fluxes. The function$f(\cdot)$denotes the simulated water or carbon flux (e.g., *R*, *ETa*, *GEP*, *NEP*), and t_b and t_f represent the baseline and future period, respectively. Thus,$f(C^{t_b}, L^{t_b})$and$f(C^{t_f}, L^{t_f})$refer to WaSSI-PRB simulations under baseline and future periods, where all climate and land use drivers are held as their baseline values. The isolated impact of an individual factor,E_{C_i} or $E_{L_j}$is estimated using a fixing-changing scenario in which only the factor under investigation is modified to its future state, while all other variables are held as their baseline levels, as:

$$EC_i = f\left(C_i^{t_f}, C_{-i}^{t_b}, L^{t_b}\right) - f(C^{t_b}, L^{t_b}), and EL_j = f\left(C^{t_b}, L_j^{t_f}, L_{-j}^{t_b}\right) - f(C^{t_b}, L^{t_b}) \tag{8}$$

where$C_i^{t_f}$and$L_j^{t_f}$represent the future values of the *i*-th climate and *j*-th land use driver, respectively;C^{t_b}andL^{t_b}denote all climate and land use drivers held at their baseline levels. And $C_{i-}^{t_b}$ and$L_{j-}^{t_b}$ denote all other climate (i.e., all components except but driver *i or j*) and land use variables held at their baseline levels.

The effect of interaction term (E_{Int}) is calculated as the difference between the total change (ΔE) and the sum of the individual contributions from all climate and land use drivers. It accounts for the nonlinear coupling and synergistic effects among multiple drivers, which are not captured when factors are analyzed independently. This term ensures the closure of the attribution framework:

$$E_{\text{int}} = \Delta E - \sum_{i=1}^{n} E_{C_i} - \sum_{j=1}^{m} E_{L_j} \tag{9}$$

To facilitate comparison of the relative importance of each driver, all contributions are normalized by the total absolute change, their contributions (%) are quantified by the relative weights as:

$$S = \sum_{i=1}^{n} \left|E_{C_i}\right| + \sum_{j=1}^{m} \left|E_{L_j}\right| + |E_{Int}|,$$

$$R_{C_i} = \frac{E_{C_i}}{S} \times 100\%, R_{L_j} = \frac{E_{L_j}}{S} \times 100\% \text{and} R_{Int} = \frac{E_{Int}}{S} \times 100\% \tag{10}$$

whereR_{C_i},R_{L_j}andR_{int}represent the percentage contribution of the *i*-th climate driver and *j*-th land use driver and the interaction term (*Int*), respectively. In addition, we define the dominant driving factor is defined as the individual main-effect driver with the largest relative absolute contribution$|R_x|$among {*PRE* , *PET*, *BAR*, *CRO*, *FOR*, *GRA*, *URB*, or *WAT*, but *Int*}.

For each SSP–RCP scenario (SSP126, SSP370, SSP585), we designed attribution experiments to quantify the contributions of two climate drivers (*PRE* and *PET*) six land use drivers (*CRO*, *FOR*, *GRA*, *URB*, *WAT*), and barren (*BAR*)) to changes in water and carbon cycles for the PRB in the NF (2021–2050) and FF (2071–2100). The rationale for these experiments settings is outlined as follows:

1. **Selecting *PRE* and *PET* as climate drivers**. *PRE* and *PET* are selected among all climatic variables due to these two drivers show lower intercorrelation and can be treated as relatively independent drivers (Chen and Buchberger, 2018; Roderick and Farquhar, 2011). Moreover, existing studies indicate that, compared to other meteorological variables such as *Tmax*, *Tmin*, *VPD* and downward shortwave radiation (*Srad*), *PET* has a strong association with the carbon sequestration capacity (Chen et al., 2025; Zhang et al., 2023). In the PET experiment, we calculate *PET* with the PM method from future meteorology (*Tmax, Tmin*, surface pressure, wind speed, *Srad*, relative humidity). Consequently, the effect of *PET* represents an integrated response to multiple underlying climate drivers. To maintain internal consistency, derived variables—e.g., *VPD* in the carbon cycling module, computed from the same future temperature and relative humidity—are updated accordingly, while other forcings remain unchanged. Correspondingly, in the *PRE* experiment, only precipitation is updated to its future values, whereas *PET* and the other variables are held at their baseline (Fig. S3a).
2. **Quantifying the impact of individual land use classes.** Within each sub-basin, the total area is conserved, while the LAI values and impervious fraction associated with each land use class are kept consistent with their baseline characteristics. For a given focal land use class *j* (e.g., forest, urban), changes are derived from spatial overlays between the baseline map (2010) and the projected NF (FF) maps at the grid-cell level. The overlays identify the donor classes converting to the focal class (A_j^+) and the recipient locations where the focal class contracts (A_j^-). Only focal–other conversions ($A_j^+ \cup A_j^-$) are retained, while conversions among the other non-focal classes remain at their 2010 levels. This design is illustrated conceptually in Fig. S3b.

Furthermore, to address the inherent uncertainties associated with relying on a single model, we adopt a multi-model ensemble approach. For each SSP-RCP scenario, WaSSI-PRB is driven separately by meteorological forcings from five GCMs, each paired with its corresponding land use projection. The arithmetic mean of the five simulations is used as the ensemble mean for that scenario and serves as the basis for subsequent analyses of future water-carbon flux dynamics and driver attributions.

4. Results

4.1. Future climate and land use changes

4.1.1. climate change

According to the ensemble mean of the five GCMs, long-term projections (2015–2100) indicate upward trends in annual *T*, *VPD*, *PRE*, and *PET* across the PRB, with magnitudes and spatial patterns varying by scenario (Fig. 3a1-d1; Fig.S4). Specifically, the growth rates of *T*, *VPD*, and *PET* increase with higher emission scenarios, being lowest under SSP126 and highest under SSP585. The corresponding ranges are 0.011–0.063 $^{\circ}C \cdot yr^{-1}$ (*T*), 0.0003–0.0047kPa$\cdot yr^{-1}$ (*VPD*), and 0.95–3.48 mm$\cdot yr^{-1}$ (*PET*) (Fig. 3a1, b1, d1). Notably, these increases are most pronounced in the northern sub-basins, where local rates exceed 0.069 $^{\circ}C \cdot yr^{-1}$, 0.0060 kPa$\cdot yr^{-1}$, and 4.17 mm$\cdot yr^{-1}$ under SSP585 (Fig. S4a6, b6, d6). By comparison, *PRE* increases more modestly, with the highest rate under SSP585 (3.07 mm$\cdot yr^{-1}$), while the lowest rate occurs under SSP370 (2.79 mm$\cdot yr^{-1}$). Spatially, increases are higher in the eastern PRB, particularly the DJRB, and lower in the western XJRB (Fig. 3c1; Fig. S4c4-c6).

Fig. 3a2-d2 and Fig. 4 summarize relative changes of four climate variables in the NF (2021–2050) and FF (2071–2100) relative to the baseline (1985–2014). In NF, relative changes are moderate. *T* and *PET* show consistent increases, ranging from 9% to 10% and 4–9%, respectively, whereas *VPD* slightly declines (<5%) (left half of the Fig. 3a2, b2, d2). By contrast, PRE exhibits small but scenario-dependent changes, with a slight decrease (0.3%) under SSP370 and modest increases (6% under SSP126 and 3% under SSP585) in the other scenarios (left half of Fig. 3c2).

In contrast, almost all climate variables exhibit substantial increases in the FF compared to the baseline, with the exception of *VPD* under SSP126. Under SSP585, *T*, *VPD*, *PRE*, and *PET* are projected to rise by 27%, 37%, 14%, and 26%, respectively (right half of Fig. 3a2-d2). These increases are most pronounced in the upper reaches of the XJRB, highlighting a robust pattern of warming and wetting and enhanced evaporative demand across the PRB. Notably, under the lowest emission scenario (SSP126), *VPD* decreases markedly in the eastern PRB, yielding a basin-wide decline (<5%). This *VPD* reduction aligns with enhanced moisture transport and higher *PRE*, whereby actual vapor pressure outpaces the warming-driven rise in saturation vapor pressure. Given that *PET* is computed using the PM method, the overall pattern suggests that increases in *PET* are driven primarily by higher net radiation and temperature, with a secondary contribution from atmospheric dryness.

4.1.2. Land use change

Future land use patterns are projected to show a net expansion of forest and urban, with corresponding declines in grassland and cropland across the PRB (Fig. 5; Fig. S5). In the baseline (2010), the land cover comprised forest (43.1%), grassland (41.8%), cropland (11.8%), water (0.7%), urban (2.6%) and barren (0.1%). By 2050, forest and urban proportions are projected to range from 48.8% to

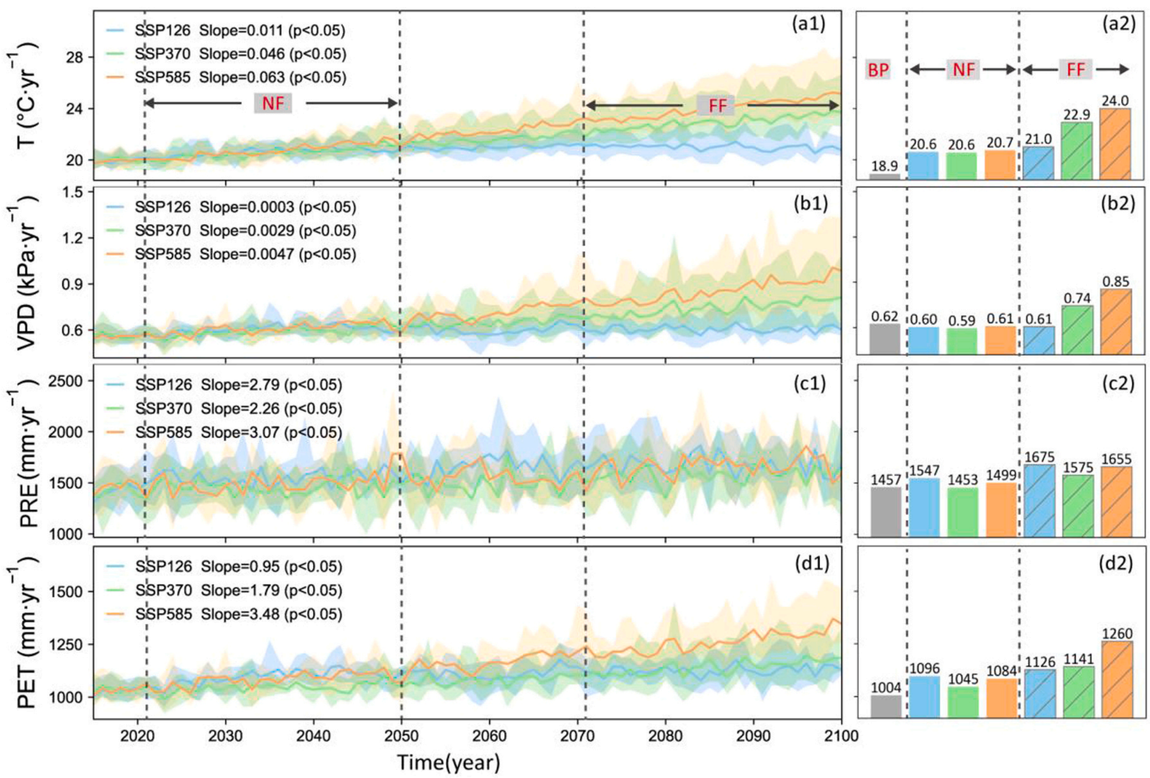

Fig. 3. Projected trends of climate variables in the PRB under SSP-RCP scenarios from 2015 to 2100. Panels (a1-d1) show the variation in annual temperature (*T*), vapor pressure deficit (*VPD*), precipitation (*PRE*), and potential evapotranspiration (*PET*), where solid lines represent ensemble mean of the five GCMs, shaded bands indicate the full inter-model range, and slopes reflect long-term linear trends estimated by ordinary least squares (OLS), with significance assessed by a two-sided *t*-test ($p < 0.05$). Panels (a2-d2) represent the mean annual values in all climate variables during the baseline period (BP: 1985–2014), near future (NF: 2021–2050), and far future (FF: 2071–2100). Bar colors in (a2-d2) correspond to SSP126, SSP370, and SSP585, following the same color scheme as in (a1-d1). Dashed lines indicate the boundaries between time periods.

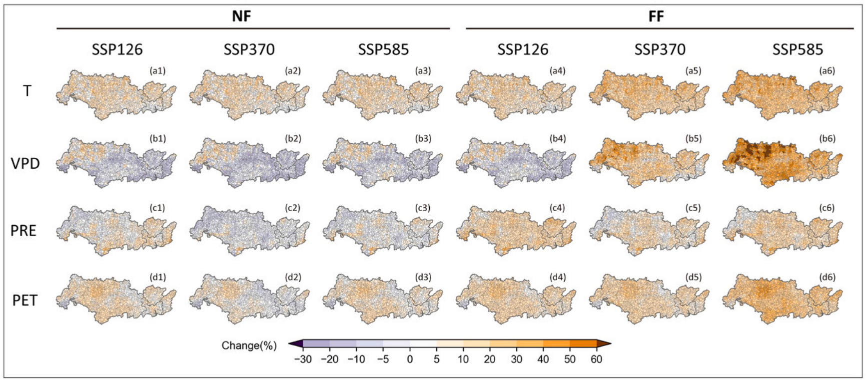

Fig. 4. Spatial distribution of the relative changes $\left(\frac{NF-BP}{BP} \times 100\% \ or \ \frac{FF-BP}{BP} \times 100\%\right)$ in climate variables across the PRB under SSP-RCP scenarios during the NF and FF, relative to the BP.

53.4% and 2.8–3.1%, respectively, both exhibiting significant increases relative to baseline. In contrast, grassland and cropland fractions are projected to decline, ranging from 36.4% to 39.0% and 10.9–4.0%, respectively. Notably, after 2050, forest, grassland, and cropland continue to change substantially, whereas urban expansion slows and tends to stabilize. By 2100, the projected proportions are 49.4–58.8% (forest), 2.8–3.1% (urban), 29.9–40.4% (grassland), and 1.3–10.5% (cropland). In addition, Sankey diagram (Fig. 5b) further reveal the dominant land use transitions across the PRB. Grassland is primarily converted to forest, while cropland is predominantly transformed into grassland, particularly in the XJRB. In contrast, urban expansion occurs mainly at the expense of grassland, with the most intensive encroachment observed in the PRD.

4.2. Future water and carbon fluxes changes

4.2.1. water fluxes change

Figs. 6–7 and Fig. S6 illustrate the projected evolution of *ETa*, *R*, and *SM* across the PRB under the combined impacts of climate and

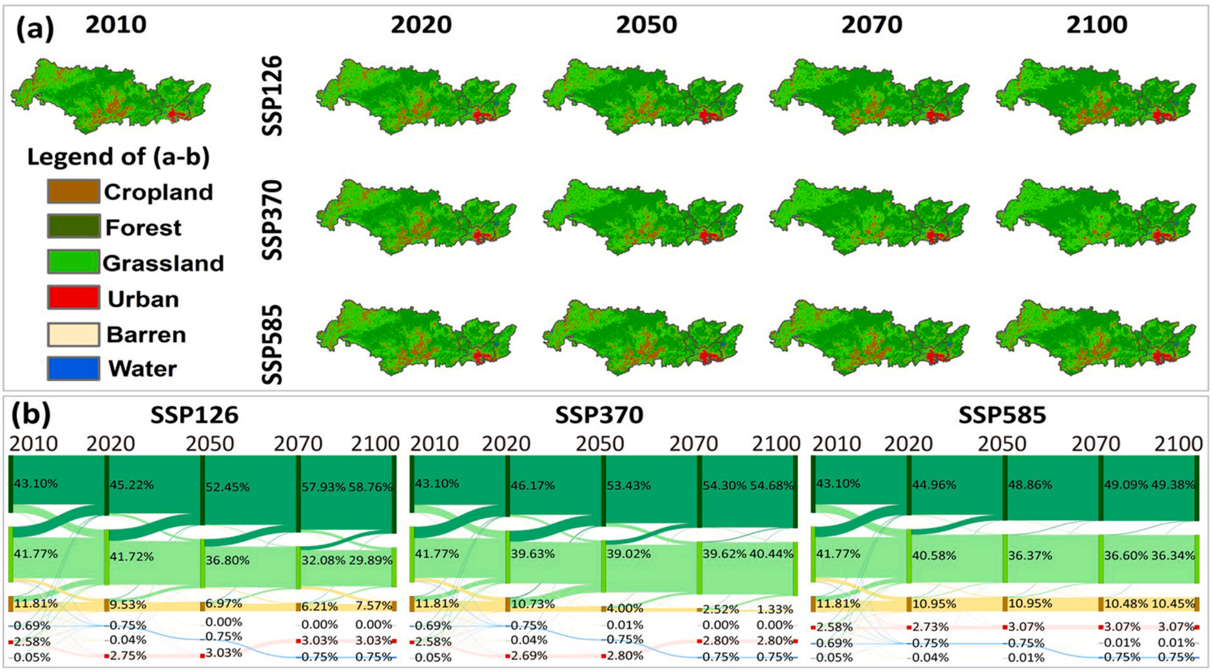

Fig. 5. Land use spatial distribution (a) and transition trajectories (b) in the PRB under SSP-RCP scenarios during the baseline year (2010) and future periods (2020–2100). Panel (a) shows the spatial patterns of six land- use classes: *CRO*, *FOR*, *GRA*, *URB*, *BAR*, and *WAT*. Panel (b) illustrates the temporal evolution and percentage transitions of each land use category across time slices under all scenarios. Fig. S5 shows the land- use changes in the PRB and its four major sub-regions from 2015 to 2100.

land use changes. From 2015–2100, *ETa* and *R* exhibit clear upward trends, with growth rates ranging from 0.93 to 1.50 $mm\cdot yr^{-1}$ and 1.23–1.67 $mm\cdot yr^{-1}$, respectively. Unsurprisingly, the highest increase for both is observed under SSP585, whereas the lowest is found under SSP126 (Fig. 6 a1, b1). Spatially, the most pronounced increases in *ETa* occur in the lower XJRB and DJRB, whereas the largest increases in *R* are generally concentrated in the DJRB and PRD (Fig. 7 a6, b6). However, *SM* remains relatively stable throughout the period, fluctuating between 310 and 360 mm, without a discernible trend (Fig. 6 c1; Fig. S6 c1-c6)

Relative to the baseline, projections indicate slight basin-wide increases in *ETa*, whereas *R* shows stronger scenario dependence and *SM* tends to decline under most scenarios in NF. Specifically, *ETa* increases range from 0.5% to 5% across the PRB (left half of the Fig. 6 a2). Meanwhile, we observed that *R* increases by 2% under SSP585 and 7% under SSP126 across the PRB (left panel of Fig. 6 b2). However, several upper XJRB sub-basins exhibit declines of 10–20%, particularly under SSP370, resulting in an overall basin-wide

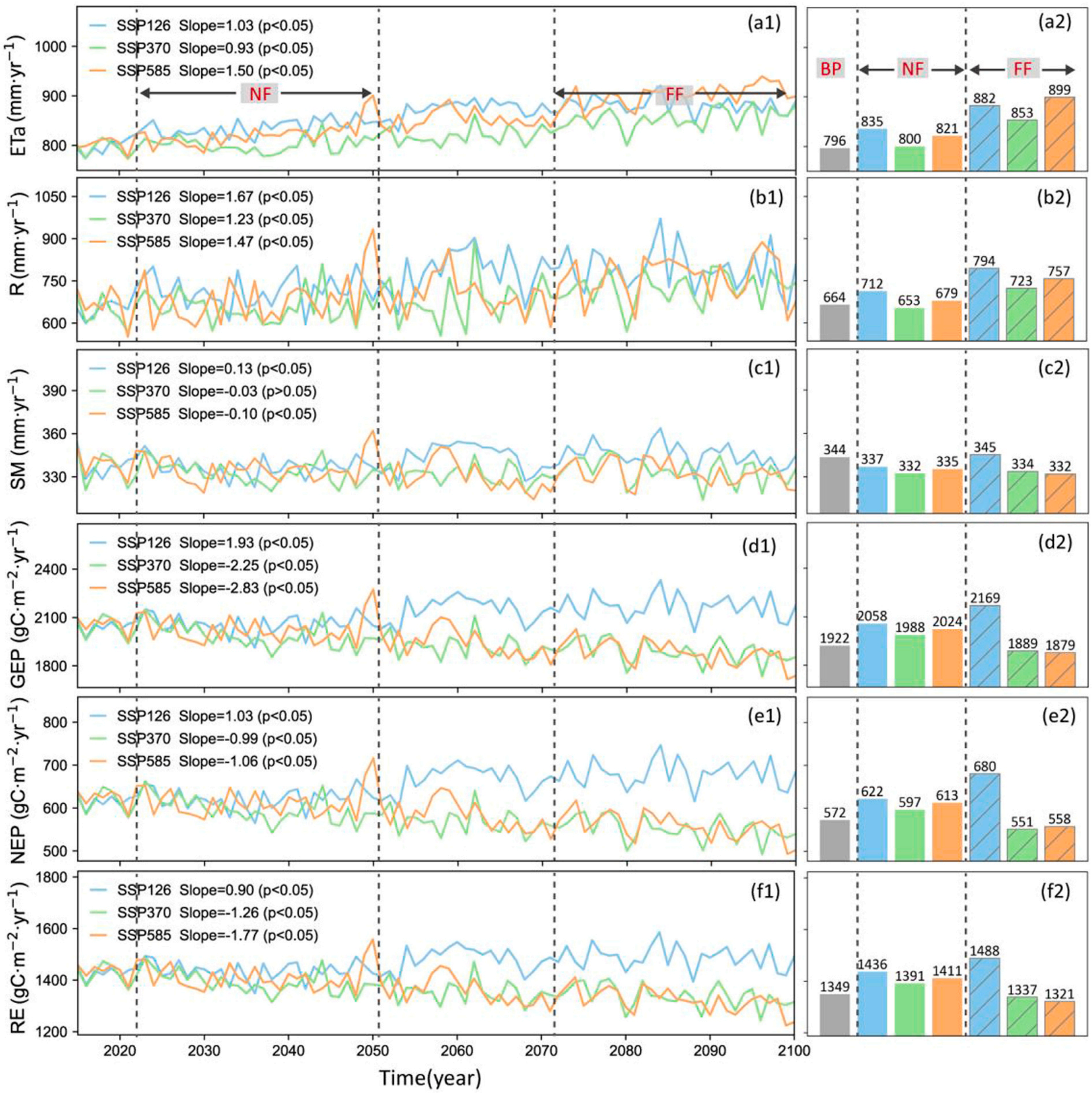

Fig. 6. Projected trends of water and carbon fluxes (ensemble mean of five GCMs) in the PRB under SSP-RCP scenarios from 1984 to 2100. Panels (a1-f1) show the variation in water fluxes, including actual evapotranspiration (*ETa*), runoff (*R*), and soil moisture (*SM*), and in carbon fluxes, including gross ecosystem productivity (*GEP*), net ecosystem productivity (*NEP*), and ecosystem respiration (*RE*); and slopes reflect long-term linear trends estimated by OLS from 2015 to 2100, with significance assessed by a two-sided *t*-test ($p < 0.05$). Panels (a2-f2) represent the mean annual values during the BP, NF, and FF. Bar colors in (a2-f2) correspond to SSP126, SSP370, and SSP585, following Bar colors in (a2-f2) correspond to SSP126, SSP370, and SSP585, following the same color scheme as in (a1-f1).

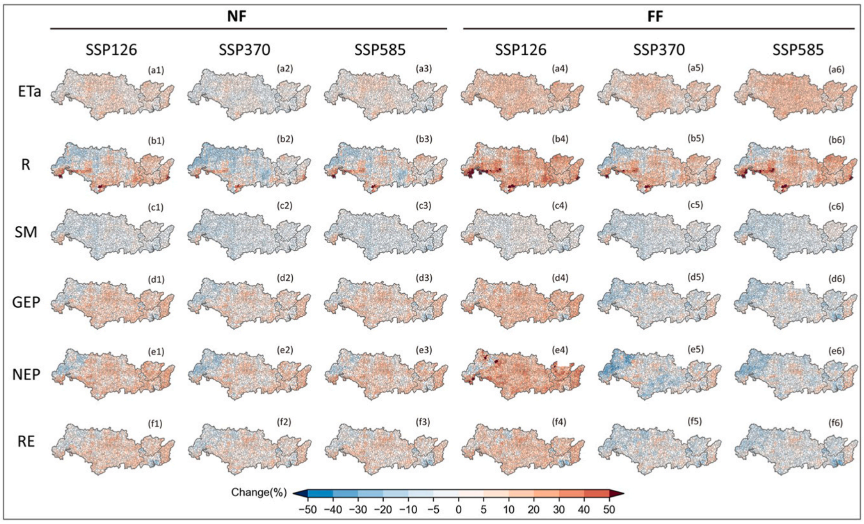

Fig. 7. Spatial distribution of the relative changes $\left(\frac{NF-BP}{BP} \times 100\% \text{ or } \frac{FF-BP}{BP} \times 100\%\right)$ in water and carbon fluxes across the PRB under SSP-RCP scenarios during the NF and FF, relative to the BP.

decrease of approximately 2% in *R* under SSP370 (Fig. 7 b2). In contrast, *SM* shows a slight overall reduction, with marginal increases observed only in parts of the lower XJRB and DJRB (Fig. 7 c1-c3). These localized gains are insufficient to offset broader losses, leading to basin-wide declines of 2–3% (left half of Fig. 6 c2). In FF, both *ETa* and *R* exhibit substantial increases of 7–13% and 14–19%, respectively (right panels of Fig. 6a2 and b2). Notably, under SSP585, increases in *ETa* of 20–30% are widespread across PRB sub-basins (Fig. 6a3), and *R* increases exceed 40% in parts of the eastern XJRB under SSP126 (Fig. 6b1). In contrast, *SM* continues to show a slight decline under both SSP370 and SSP585 (right panel of Fig. 6 c2; Fig. 7 c1–6c3).

4.2.2. Carbon fluxes change

Figs. 6, 7, and S6 also indicate that basin-wide *GEP*, *NEP*, and ecosystem respiration (*RE*) increase under SSP126, whereas they decline under the higher emission scenarios (SSP370 and SSP585) from 2015 to 2100 across the PRB. Under SSP126, most sub-basins exhibit increasing trends in *GEP*, *NEP*, and *RE*, with localized declines confined to the lower PRD (Fig. S6 d4, e4, and f4), resulting in basin-mean growth rates of 1.93, 1.03, and 0.90 $gC·m^{-2}·yr^{-1}$ for *GEP*, *NEP*, and *RE*, respectively. In contrast, under SSP370 and SSP585, all three fluxes decline, with *GEP*, *NEP*, and *RE* decreasing by 2.25–2.83 $gC·m^{-2}·yr^{-1}$, 0.99–1.06 $gC·m^{-2}·yr^{-1}$, and 1.26–1.77 $gC·m^{-2}·yr^{-1}$, respectively. These reductions are most pronounced in the middle and upper XJRB (Fig. S5d6, S5e6, and S5f6), highlighting the region's heightened sensitivity to long-term climate and land use changes.

Specifically, relative to the baseline, carbon fluxes across the PRB are projected to increase under all emission scenarios, indicating a basin-wide enhancement in ecosystem carbon uptake and productivity in NF (left panels of Fig. 6 d2, e2, and f2). Under SSP126, the increases are most pronounced, with *GEP*, *NEP*, and *RE* rising by 7%, 9%, and 7%, respectively. By comparison, under the higher emission scenarios (SSP370 and SSP585), increases are smaller but remain evident, typically 3–5% across the three fluxes. Although the basin-mean signals are positive, localized stagnation or slight declines persist in several sub-basins of the upper XJRB and the lower PRD (Fig. 6 d1-d3, e1- e3, f1-f3).

However, the results suggest that terrestrial carbon sequestration capacity is weakened in the PRB in FF under higher emission scenarios (right panels of Fig. 6 d2, e2, and f2). Under SSP126, basin-wide *GEP*, *NEP*, and *RE* increase by 13%, 19%, and 10%, respectively, reflecting continued enhancement of ecosystem productivity and carbon cycling under lower-emission conditions. In contrast, *GEP*, *NEP*, and *RE* decline by approximately 2%, 3%, and 1%, respectively, under SSP370 and SSP585. Notably, this decline in *NEP* is attributed to the mechanism whereby the increase in *RE* outpaces that of *GEP*. Spatially, the most pronounced decreases occur in the upper XJRB, where *NEP* drops by more than 40% (Fig. 7 e5-e6). This pattern is consistent with stronger warming and evaporative demand, which amplifies *RE* relative to *GEP* in water-limited sub-basins and thereby reduces *NEP*.

4.3. Attribution of climate and land use impacts on water and carbon fluxes

4.3.1. Contributions of individual driving factors

Based on the attribution experiments in Section 3.4, we quantify the contributions of climate and land use drivers to water and carbon fluxes for the PRB and its four sub-regions in both NF and FF, with results summarized in Fig. 8 and detailed in Figs. S7-S8. Overall, future changes feature notable offsetting among drivers. Climate drivers exert far stronger control on water fluxes than land use, whereas land use drivers play a comparatively more pronounced role for carbon fluxes, especially in NF.

Changes in water fluxes are predominantly driven by climate drivers across the PRB (Fig. 8 a1-c4 in the PRB). Under most future scenarios (except for NF-SSP370), both *PRE* and *PET* increase, establishing a robust climate-dominance pattern in hydrological responses.

Specifically, *ETa* rises due to concurrent positive contributions from *PRE* (10–52 mm·yr^{-1}, 19–45%) and *PET* (25–68 mm·yr^{-1}, 32–55%); *R* is primarily enhanced by *PRE* (32–166 mm·yr^{-1}, 61–80%), while *PET* exerts a negative feedback (−57 to −16 mm·yr^{-1}, −30 to −13%) by elevating atmospheric evaporative demand and partially offsetting the *PRE*-driven increase. *SM* is co-modulated by PRE (3–15 mm·yr^{-1}, 20–53%) and *PET* (−18 to −5 mm·yr^{-1}, −57 to −28%), whose opposing effects largely offset each other, resulting in minimal net change. However, under the NF-SSP370 scenario, where *PET* continues to rise while PRE slightly declines, the typical offsetting balance is disrupted. Specifically, the reduction in PRE exerts consistent negative effects on *ETa* (−2 mm·yr^{-1}, −6%), *R* (−2 mm·yr^{-1}, −9%), and *SM* (−2 mm·yr^{-1}, −17%). Meanwhile, *PET* maintains the sign of its impact on these water fluxes, continuing to enhance *ETa* while suppressing *R* and *SM.*

In contrast, land use drivers play secondary roles overall but exhibit marked differentiation in their effects on water fluxes. Changes in FOR or GRA contribute positively to ETa (typically within 10%), while exerting negative effects on R and SM, generally ranging from −5–0% and from −7% to −3%, respectively. CRO exhibits similar directional effects on the three fluxes as FOR and GRA but with smaller magnitudes. URB contributes positively to R (≤3%) but slightly reduces ETa (approximately −2%) and SM (−4% to −2%). BAR and WAT show effects of similar sign to URB but are negligible in magnitude.

We further investigate the impacts of various driving factors on basin-wide carbon fluxes (Fig. 8 d1-f4 in the PRB). At the PRB scale,

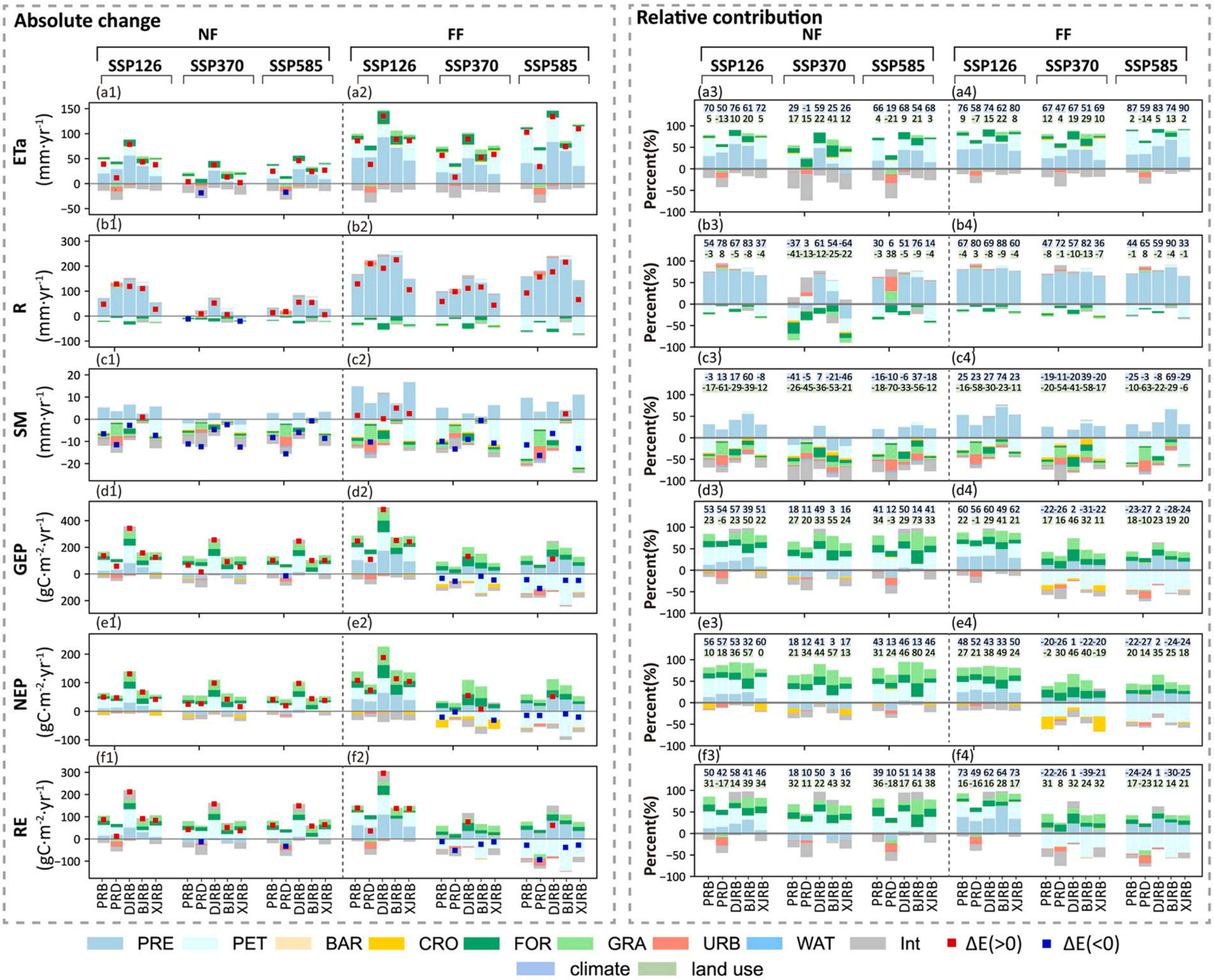

Fig. 8. Impacts of individual drivers on water and carbon fluxes in the PRB and its four sub-regions under SSP-RCP scenarios during the NF and FF, relative to the BP. Panels (a1-a2, b1-b2, c1-c2) show absolute changes in *ETa*, *R*, and *SM* (mm·yr^{-1}); panels (d1-d2, e1-e2, f1-f2) show absolute changes in *GEP*, *NEP*, and *RE* (gC·m^{-2}·yr^{-1}). Absolute changes are attributed to individual driving factors using the fixing-changing approach (Eqs. (7)-(9)). Panels (a3-a4, b3-b4, c3-c4) and (d3-d4, e3-e4, f3-f4) indicate the contributions (%) of each driving factor to the total change in the respective fluxes, computed with Eq. (10). *PRE* , *PET*, *BAR*, *CRO*, *FOR*, *GRA*, *URB*, *WAT*, and *Int* denote the contributions attributable to changes in precipitation, potential evapotranspiration, barren land, cropland, forest, grassland, urban land, water bodies, and interactions among drivers, respectively. Δ*E* denotes the net change in each flux. "climate" denotes the sum of contributions from *PRE* and *PET*, and "land use" denotes the sum from *BAR*, *CRO*, *FOR*, *GRA*, *URB*, and *WAT*. Detailed values are provided in Figs. S7-S8.

changes in carbon fluxes are primarily controlled by the relative strength of *PRE* and *PET,* with PET generally exerting the stronger impact. Specifically, increases in *PRE* positively influence carbon fluxes in all future scenarios except for NF-SSP370, where a slight decline in *PRE* leads to reduced carbon fluxes. Meanwhile, although *PET* rises markedly in all future scenarios, its effect exhibits clear scenario dependence: in NF, higher *PET* enhances carbon fluxes by strongly increasing *ETa* under all SSP-RCP scenarios; however, in FF under medium-to-high emission scenarios (SSP370 and SSP585), persistently elevated *PET* induces hot-dry atmospheric, leading to a pronounced suppression of carbon fluxes. Notably, land use drivers also exert a significant influence on carbon fluxes: *FOR* and *GRA* typically provide a stable enhancement, while *CRO* shows a more prominent negative effect. Given the functional coupling of *GEP*, *RE*, and *NEP* in our framework (Eqs. (5)-(6)), factor-specific effects are largely consistent across all three carbon fluxes.

We therefore focus on *NEP (*Fig. 8 e1-e4 in the PRB), which directly represents the net carbon balance, with detailed *GEP* and *RE* results provided in Fig. 8 e1-e4 and Fig. 8 f1-f4, respectively. As an illustrative example, relative to the baseline, under NF-SSP126, *NEP* is projected to increase by 50 gC·m^{-2}·yr^{-1}. Of this increase, *PET* and *PRE* contribute +34 gC·m^{-2}·yr^{-1} (43%) and +10 gC·m^{-2}·yr^{-1} (13%), respectively; *FOR* and *GRA* contribute approximately +9 (12%) and +11 (14%) gC·m^{-2}·yr^{-1}, while *CRO* contributes −10 gC·m^{-2}·yr^{-1} (−13%). However, under FF-SSP585, *NEP* decreases by 15 gC·m^{-2}·yr^{-1}. Although *PRE* , *FOR*, and *GRA* provide positive contributions of +28 (21%), +11 (8%), and +20 (15%) gC·m^{-2}·yr^{-1}, these gains are insufficient to offset the *PET*-driven suppression (−58 gC·m^{-2}·yr^{-1}, −44%) and the negative *Int* (−12 gC·m^{-2}·yr^{-1}, −9%). Additional minor negative contributions from *BAR*, *URB*, and *WAT* further reinforce the overall decline in *NEP*.

Basin-scale generalization is insufficient to capture the spatial heterogeneity of driving mechanisms on water and carbon fluxes. We therefore reveal significant spatial differentiation at the sub-regional scale, which is primarily attributed to the modulatory effects of land use change (Fig. 8 a1-f4 in the four sub-regions). For instance, in the PRD, urban expansion yields a positive *URB* contribution to *R* (up to 34% under NF-SSP585) and a negative *URB* contribution to *NEP* (up to −8% under FF-SSP585), highlighting coupled runoff amplification and carbon-sink suppression (Fig. 8 b3 and e4 in the PRD). Meanwhile, *FOR* and *GRA* exert stronger effects in the DJRB and BJRB, yielding a pattern of hydrological reduction coupled with enhanced carbon sequestration. Specifically, the effect of *FOR* on *R* is most negative under NF-SSP370, reaching −14% and −16% in the DJRB and BJRB, respectively (Fig. 8 b3 in the DJRB and BJRB). And the effects of *FOR* and *GRA* contribute positively to *NEP* across all scenarios—for example, their contributions peak at 31% (*FOR*) and 50% (*GRA*) in the BJRB under NF-SSP585 and at 23% (*FOR*) and 30% (*GRA*) in the DJRB under FF-SSP370 (Fig. 8 e3 in the BJRB and e4 in the DJRB). Furthermore, in the XJRB, the sustained reduction in cropland area under SSP370 leads to a markedly negative effect of *CRO* on *NEP*, with a maximum contribution of −35% (FF-SSP370), establishing it as a key driver of the sub-region's long-term decline in carbon sequestration (Fig. 8 e4 in the XJRB).

4.3.2. Spatial distribution of dominant driving factors

To further investigate the spatial pattern of future climatic and land use impacts on water and carbon fluxes at the sub-basin scale, we mapped the spatial distribution of dominant driving factors (Eq. 10) and summarized their areal coverage (Fig. 9; Fig. S9).

The dominant drivers of *R* exhibit pronounced climate-driven homogeneity (Fig. 9b1-b6; Fig. S9b1-b6). Under most scenarios, climate drivers collectively control more than 90% of the PRB area, with *PRE* alone consistently exceeding 70%. In contrast, the dominant proportion of *PET* remains approximately 12–24% (except for under NF–SSP126), concentrated mainly in the upper XJRB.

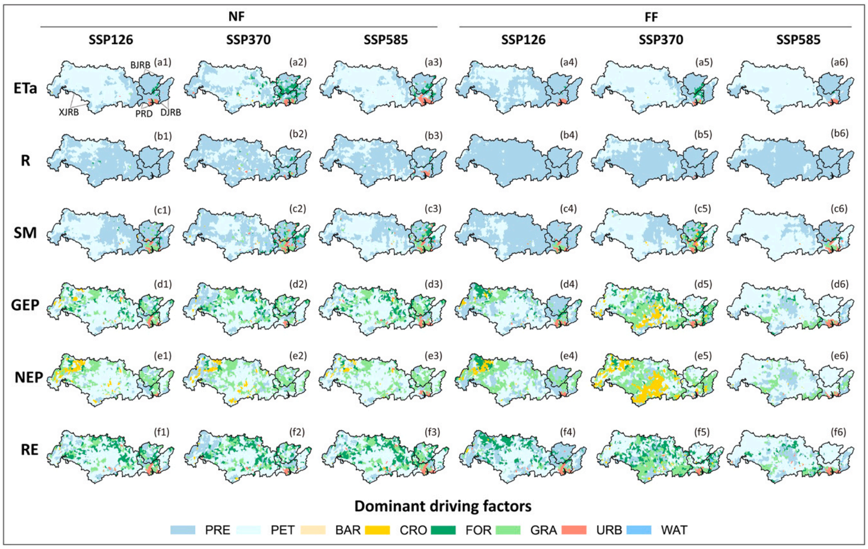

Fig. 9. Dominant driving factors impacting water and carbon fluxes in the PRB and its four major sub-regions under SSP-RCP scenarios in NF and FF, relative to the BP. Panels (a1-f6) show the spatial distribution of dominant driving factors for each sub-basin. Figs. S9 illustrates the areal proportions (%) of different dominant driving factor across the PRB, PRD, DJRB, BJRB, and XJRB. Definitions of all variables and contributing factors follow those in Fig. 8.

Additionally, *URB*-dominated areas are discernible in the PRD, accounting for up to 11% of the PRD area under NF-SSP585.

Compared with the spatial pattern for *R*, those for *ETa* and *SM* exhibit a clear partitioning between climate drivers, with *PET* occupying a markedly larger proportion. For *ETa*, *PET*-dominated areas cover more than 50% of the PRB area and are projected to expand further under higher emission scenarios, predominantly distributed in the XJRB (Fig. 9a1-a6; Fig. S9a1-a6). In contrast, *PRE*-dominated areas remain relatively stable at approximately 30% of the PRB, primarily in the more humid DJRB and BJRB. Effects of land use drivers on *ETa* are particularly pronounced along the transition zone between the PRD, DJRB, and BJRB, where *FOR*-dominated areas reach their maximum extent under NF-SSP370, accounting for 25%, 21%, and 38% of the PRD, DJRB, and BJRB areas, respectively. Moreover, in the lower PRD, *URB*-dominated areas account for approximately 13–27% of the region. Similarly, the overall dominance pattern for *SM* resembles that of *ETa* but exhibits regional distinctions (Fig. 9c1-c6; Fig. S9c1-c6). Specifically, *PRE*-dominated areas are also common in the lower XJRB, in addition to clustering in the DJRB and BJRB. Land use dominated areas are more frequent in the DJRB and PRD, specifically those dominated by *GRA*, *FOR*, or *URB*.

Relative to water fluxes, carbon fluxes exhibit a substantially higher areal proportion of land use dominated areas, often exceeding 30% of the PRB area in future scenarios (Fig. 9d1-f6; Fig. S9d1-f6). Spatially, *GRA*- and *FOR*-dominated areas are more dispersed. Basin-wide, *GRA* dominance accounts for 9–26% of the PRB area for *GEP*, 13–29% for *NEP*, and 8–21% for *RE*, primarily in the middle-lower BJRB, with smaller clusters in the middle XJRB. Notably, when *FOR* is the dominant driver of *RE*, its areal proportion reaches approximately 20% of the PRB area, exceeding the corresponding proportions for *GEP* (approximately 10%) and *NEP* (<3%). Conversely, *CRO*- and *URB*-dominated areas show more concentrated patterns: *CRO* dominance clusters in the middle-lower XJRB and, for *NEP*, peaks at 26% of the XJRB area under FF-SSP370. *URB*-dominated areas are largely confined to the lower PRD, with maxima of 18%, 9%, and 21% of the PRD area for *GEP*, *NEP*, and *RE*, respectively.

5. Discussion

5.1. Strengths of the proposed attribution framework

We propose a framework to evaluate the impacts of climate and land use changes on the terrestrial water and carbon cycles under SSP-RCP scenarios. Our results confirm a widely reported finding that climate change exerts a stronger impact on basin hydrological processes than land use change under projected warmer and wetter future scenarios (Yang et al., 2019; Yang et al., 2023; Yonaba et al., 2023). In contrast, although land use change generally has a weaker impact on the carbon cycle than climate change, it can temporarily and locally exceed climate drivers, particularly in regions undergoing substantial land cover transitions (Feng et al., 2023; Hou et al., 2022; Xu et al., 2022). However, prior studies typically treated climate and land use changes as aggregated categories and lacked a unified framework for quantitatively attributing changes to individual drivers. Our attribution framework overcomes this limitation by explicitly disentangling climate into *PRE* and *PET* and land use into six classes, and quantifying the contribution of each driver separately. For example, in the PRB, we disentangle projected increases in *R* across scenarios and attribute them primarily to positive contributions from higher *PRE* and urban expansion, which together outweigh the main negative contributions from *PET* and changes in forest and grassland (Fig. 8b1-b4).

Moreover, our framework reveals that PET impacts on regional carbon sinks are highly scenario-dependent (see Section 4.3.1). This contrasting response can be explained by the internal structure of the WaSSI-PRB carbon cycling module, which directly links *NEP* to *ETa* and *VPD*. With *uWUE* and the respiration parameters *m* and *n* held constant for each land use class, *NEP* is approximately proportional to the ratio$\mathrm{ETa}/\mathrm{VPD}^{0.5}$(Eqs. (4)-(6): $\mathrm{NEP} = (1 - \mathrm{n}) \times uWUE \times \mathrm{ETa}/\mathrm{VPD}^{0.5} - m$). In this formulation, *ETa* represents the actual evapotranspiration that supports carbon uptake through transpiration, whereas *VPD* reflects the atmospheric water stress. *NEP* therefore increases with higher *ETa* but decreases with higher *VPD*, and *PET* influences *NEP* only through its combined impacts on *ETa* and atmospheric dryness. In the NF, although *PET* increases due to warming, *VPD* remains close to the baseline (Fig.3b2), indicating that atmospheric aridity does not intensify substantially. At the same time, increased precipitation maintains relatively favorable soil moisture conditions, allowing *ETa* to respond strongly to the higher evaporative demand; as a result,$\mathrm{ETa}/\mathrm{VPD}^{0.5}$increases and *NEP* is enhanced.

In contrast, in the FF under higher emission scenarios (SSP370 and SSP585), strong warming leads to a pronounced rise in *VPD* (Fig.3b2), while soil moisture deficits emerge as higher atmospheric demand and more variable precipitation draw down soil water (Fig.3c2). Under these conditions, *ETa* becomes water-limited and can no longer keep pace with the rapidly increasing atmospheric demand, so$\mathrm{ETa}/\mathrm{VPD}^{0.5}$declines and *NEP* is suppressed despite higher *PET*, displaying a characteristic hot-dry atmospheric stress regime in which the increase in *VPD* outpaces the capacity of ecosystems to increase *ETa*. This pattern, in which enhanced evapotranspiration and apparent vegetation productivity do not necessarily convert to stronger carbon sinks under water-limited conditions, has been documented in previous studies (Chen et al., 2025; Yang et al., 2025; Yuan et al., 2019). Multiple evidence indicate that prolonged warming can substantially reduce the carbon sink capacity of terrestrial ecosystems (Tharammal et al., 2019; Uribe et al., 2023; Zeng et al., 2023).

Our framework offers actionable guidance for water and land resource managers to design integrated strategies for coordinated management of regional water and carbon cycles under SSP-RCPs. Although demonstrated for the PRB, the scalable simulation–attribution framework is transferable to other climate-sensitive, human-impacted regions worldwide, including the Loess Plateau (Zhang et al., 2023) and the Yangtze River Basin (Zhang et al., 2022; Liu et al., 2025) in China, the U.S. Colorado River Basin (Whitney et al., 2023), the Mississippi River Basin (Dannenberg et al., 2025), and South Asia's Ganges-Brahmaputra-Meghna Basin (Qiu et al., 2025; Amjath-Babu et al., 2025).

5.2. Comparison with previous studies in the PRB

The PRB is an economically significant region in southern China with high ecological value and critical water conservation functions, making its hydrology and ecosystem services particularly sensitive to environmental change (Li et al., 2023; Qi et al., 2023, 2024; Wu et al., 2020). Over recent decades, temperature has risen while *PRE* has remained relatively stable (Tang et al., 2024; Tian and Yang, 2017), and land use has shown a dual trajectory of urbanization and greening: large-scale vegetation restoration has increased greenness upstream, whereas urbanization and industrialization downstream have expanded impervious surfaces and degraded vegetation (He et al., 2021; Wang et al., 2021; Yang et al., 2021). Budyko-based analyses generally report that climate factors dominate changes in *R*, with beneficial *PRE* effects offset by adverse contributions from *PET* and surface parameters, yielding only a slight downward trend in *R* over past decades (Yang et al., 2022; Yin et al., 2023).

Our projections confirm that climate remains the primary driver of future *R* variability, consistent with recent projections (Zhang and Gan, 2025). By quantifying driver-specific contributions at the basin scale, we find that *PRE* dominant 60–80% of projected *R* increases across scenarios—while rising *PET* consistently offsets 13–30%. Land use change is secondary, with individual contributions typically within the ±5% range, although urban expansion can significantly increase *R* locally in sub-regions such as the PRD. Furthermore, our attribution framework offers a robust basis for quantifying the individual impacts of land use drivers on the basin-scale carbon cycle. Xu et al. (2023) reported that the Pearl River Protection Forest Program (since 1996) was associated with a reversal in *NEP* from a declining to an increasing trend, highlighting the positive role of forest and grassland expansion in enhancing regional carbon sinks. Consistent with this historical evidence, our forward-looking analysis indicates that projected increases in forest cover will enhance basin-wide *NEP* under future scenarios (see factorial experiments in Section 4.3.1).

It is important to note that the role of forest cover in modulating basin water yield remains debated (Ellison et al., 2012; Farley et al., 2005; Filoso et al., 2017; Hoek van Dijke et al., 2022). Our findings indicate that forest expansion can exert a material influence on *R* in certain sub-basins of the PRB. Specifically, increased forest cover is projected to reduce *R* in the DJRB and BJRB, with forest-related contributions ranging from −13.5% to −4.4% and from −16.4% to −3.5%, respectively. These results align with earlier studies reporting negative hydrological impacts of afforestation in similar settings (Bai et al., 2020; Liu et al., 2016; Zhang and Hao, 2025). In contrast, some investigations based on trend analysis or elasticity methods indicate that large-scale forest restoration in humid regions of southern China has not resulted in a statistically significant reduction in regional water yield (Li et al., 2021; Xue et al., 2022; Zhou et al., 2010). This apparent discrepancy may stem from methodological limitations, as such approaches typically isolate climate effects first and subsequently attribute residual changes to land use, thereby overlooking potential interactions between climate variability and vegetation dynamics, such as offsetting or synergistic effects (Li et al., 2017; Wei et al., 2013; Wei et al., 2018; Wei and Zhang, 2010). By explicitly accounting for these coupled processes through factorial scenario experiments, our framework captures the hydrological response to forest change under evolving climatic conditions. This mechanistic treatment helps reconcile divergent findings in the literature and supports the view that forest ecosystems can reduce *R* through enhanced canopy interception, evaporation, and transpiration (Onuchin et al., 2018, 2021), particularly in basins where vegetation change coincides with pronounced climatic shifts.

5.3. Limitations and future perspectives

Although our proposed framework effectively projects future trajectories of basin-scale water and carbon cycles and quantitatively disentangles the individual and combined contributions of climate and land use changes, several limitations and associated uncertainties warrant acknowledgment. Based on the WaSSI-PRB model, our approach incorporates several key improvements, including the replacement of the Hamon formula with the PM method for PET estimation and the refinement of *GEP* calculations via *VPD* and *uWUE*. Nevertheless, uncertainties arising from model structure, parameterization, and input data quality may still influence the results (Refsgaard et al., 2006; Yen et al., 2014; Zheng et al., 2018).

Structurally, WaSSI relies on an empirical formulation for *PAET* that integrates *PRE* , *PET*, and *LAI*, but omits explicit representation of stomatal conductance and the modulating role of atmospheric CO_2 (Duarte et al., 2024; Sun et al., 2011). It also neglects dynamic feedback from time-varying soil properties and *LAI*, which may bias estimates of *R* and *GEP* (Li et al., 2020; Sun et al., 2015).

Regarding parameterization, although the SCE-UA algorithm was employed to recalibrate the four regression-derived parameters in the *PAET* equation, direct optimization within the WaSSI-PRB framework may induce overfitting and equifinality and may weaken physical interpretability (Beven and Freer, 2001; Whittaker et al., 2010). Moreover, the coarse spatial resolution of input datasets, including 5 km land use maps and 0.5° climate forcing, may limit the model's capacity to resolve sub-basin hydrological heterogeneity despite downscaling efforts, thereby propagating remote sensing-related uncertainties into the outputs (Shrestha et al., 2006). Despite these caveats, WaSSI retains practical advantages, notably its parsimonious structure and reliance on widely accessible inputs (Sun et al., 2011). Importantly, our trend-focused conclusions appear robust: prior work indicates that WaSSI's sub-basin outputs remain broadly consistent across varying land use resolutions, with minimal impact on basin-scale patterns (Bagstad et al., 2018b).

Further concerns may exit in attributing individual driver impacts on water and carbon fluxes. The improved fixing-changing method used in this study incorporates an interaction term among drivers (*Int*; gray legend in Fig. 8) that absorbs cross-driver covariance to close the budget. While this improves numerical closure, it does not resolve the underlying interaction mechanisms, so estimated relative contributions of single drivers may carry uncertainty where interactions are strong. Future work should aim to further elucidate the interaction mechanisms among drivers. An alternative approach would be to draw on the research ideas of Liu et al. (2019) and Yang et al. (2017) to optimize and enhance the existing fixing–changing method, thereby improving the accuracy and reliability of quantitative results.

6. Conclusions

Climate and land use jointly shape regional water-carbon cycles, and distinguishing their respective impacts is essential for sustaining long-term water-carbon balance. To achieve that, we develop an integrated simulation-attribution framework that couples the WaSSI-PRB model with an improved fixing-changing approach to quantify drivers' separate and offsetting impacts. Applying to the humid subtropical PRB, we disentangle the individual contribution of climate drivers (*PRE* and *PET*) and land use (*CRO*, *FOR*, *GRA*, *URB*, *WAT* and *BAR*) to water (*ETa*, *R* and *SM*) and carbon (*GEP, NEP* and *RE*) fluxes under SSP126, SSP370 and SSP585 scenarios in both NF (2021–2050) and FF (2071–2100). The main conclusions are as follows:

(1) The WaSSI-PRB model (with improved water and carbon cycling modules) accurately simulates water and carbon fluxes across the PRB, validating against historical runoff observations and satellite-derived *ETa* and *GEP* products, thus can be used as a reliable tool for projecting future water–carbon dynamics.
(2) Basin-mean *T*, *VPD*, *PRE* , and *PET* are projected to increase from 2015 to 2100, with the strongest changes under SSP585 and the most pronounced trends in the northern sub-basins. Climate changes are moderate in the NF but intensify markedly in the FF comparing with the 1985–2014 baseline. Concurrently, basin's future land use shifts toward continuous afforestation alongside ongoing urbanization. Dominant transition are grassland-to-forest and cropland-to-grassland (particularly in the XJRB), while urban growth occurs mainly at the expense of grassland and is concentrated in the PRD.
(3) Projections indicate that basin-wide ETa and R appreciably increase, whereas SM shows minor changes across all scenarios. In the NF, increases in ETa and R remain modest, but they become more pronounced in the FF, especially under higher-emission scenarios. In contrast, carbon fluxes are highly scenario-sensitive: *GEP*, *NEP*, and *RE* increase by about 3–9% in the NF and strengthen further in the FF under SSP126, while only gains modestly in the NF but decline in the FF (typically $<$3%) under SSP370 and SSP585, indicating weakening carbon sequestration capacity in the PRB under higher-emission scenarios.
(4) Attributions indicate that *PRE* and *PET* jointly control water fluxes changes across the PRB, yet exhibit contrasting roles and distinct spatial patterns across different fluxes. *PRE* is the main positive driver of increases in *R* (contribution 61–80%) and dominates over 70% of the PRB area, whereas *PET* provides a negative feedback ($-$30% to $-$13%) with *PET*-dominated areas covering 12–24% (mainly upper XJRB). For *ETa*, *PET* contributes more (32–55%) and dominates over 50% of the basin (expanding under higher emissions, largely in the XJRB), while *PRE* contributes 19–45% and dominates about 30% (primarily in the DJRB and BJRB). *SM* reflects the strongly offsetting effects of *PRE* (positive) and *PET* (negative), yielding small net change and a clear climatic partition of dominance. Land use effects are limited at the basin scale but can be locally dominant: in the PRD, *URB* raises *R* by up to $+$34% under NF-SSP585 (*URB*-dominated area 11%), whereas under NF–SSP370 forest expansion reduces *R* by $-$14% and $-$16% in the DJRB and BJRB (*FOR*-dominated areas 21% and 38%, respectively).
(5) Unlike water fluxes, carbon flux changes are jointly controlled by climate and land use. *PRE* generally exerts a positive effect, whereas the *PET* effect is strongly scenario-dependent: in the NF, higher *PET* enhances carbon fluxes via increased *ETa*; in the FF under SSP370 and SSP585, persistently high *PET* induces *PET*-driven hot-dry atmospheric that suppresses *NEP* (e.g., *PET* contributes $+$43% to *NEP* under NF-SSP126 but $-$44% under FF–SSP585). Land use signals are systematic yet spatially heterogeneous: change in *FOR* and *GRA* generally enhance carbon uptake, while *URB* and *CRO* reduce it—for example, *URB* contributes up to $-$8% to NEP in the PRD (FF-SSP585), while *FOR* contributes up to 23% and 31% to NEP in the DJRB (FF-SSP370) and BJRB (NF-SSP585), respectively. Overall, regional carbon cycling is shaped by large-scale climate evolution but remains highly sensitive to human-driven land use change.

CRediT authorship contribution statement

Jiangchao Qiu: Writing – review & editing, Writing – original draft, Visualization, Validation, Methodology, Investigation, Formal analysis, Data curation, Conceptualization. **Xiaola Wang:** Writing – original draft, Visualization, Validation, Software, Methodology, Investigation, Formal analysis, Data curation, Conceptualization. **Ge Sun:** Writing – review & editing, Supervision, Software, Resources, Conceptualization. **Kai Duan:** Writing – review & editing, Validation, Supervision, Software, Resources, Project administration, Funding acquisition, Conceptualization. **Huan Liu:** Visualization, Validation, Funding acquisition, Data curation. **Jianhua Wang:** Writing – review & editing, Supervision, Resources, Project administration, Funding acquisition, Data curation. **Xuanxuan Wang:** Visualization, Validation, Supervision. **Peng Hu:** Writing – review & editing, Supervision, Resources, Methodology, Investigation, Funding acquisition, Data curation, Conceptualization.

Declaration of Competing Interest

The authors declare that they have no known competing financial interests or personal relationships that could have appeared to influence the work reported in this paper.

Acknowledgment

This work was supported by the National Natural Science Foundation of China (52379032, 52122902, 52394233), the Guangdong Basic and Applied Basic Research Foundation (2023A1515012241, 2023B1515040028), the Science and Technology Program of Guangdong (2024B1212040001), and Young Elite Scientists Sponsorship Program by CAST (2023QNRC001).

Appendix A. Supporting information

Supplementary data associated with this article can be found in the online version at doi:10.1016/j.ejrh.2026.103303.

Data availability

Data will be made available on request.

References

Allen, R.G., Pereira, L.S., Raes, D., Smith, M., 1998. Crop evapotranspiration: guidelines for computing crop water requirements. In: FAO Irrigation and Drainage Paper No, 56. FAO, Rome.

Amjath-Babu, T.S., Anwar, N.H., Chanda, A., Chaturvedi, R.K., Hina, S., Fadnavis, S., Sarathchandra, C., Shakya, S.R., Singh, C., 2025. Perspectives on climate change in South Asia. Nat. Clim. Change 16. https://doi.org/10.1038/s41558-025-02442-7.

Arantes, A.E., Ferreira, L.G., Coe, M.T., 2016. The seasonal carbon and water balances of the Cerrado environment of Brazil: past, present, and future influences of land cover and land use. ISPRS J. Photogramm. Remote Sens. 117, 66–78. https://doi.org/10.1016/j.isprsjprs.2016.02.008.

Bagstad, K.J., Cohen, E., Ancona, Z.H., McNulty, S.G., Sun, G., 2018. The sensitivity of ecosystem service models to choices of input data and spatial resolution. Appl. Geogr. 93, 25–36. https://doi.org/10.1016/j.apgeog.2018.02.005.

Bai, P., Liu, X., Zhang, Y., Liu, C., 2020. Assessing the impacts of vegetation greenness change on evapotranspiration and water yield in China. Water Resour. Res. 56 (10). https://doi.org/10.1029/2019WR027019.

Beven, K., Freer, J., 2001. Equifinality, data assimilation, and uncertainty estimation in mechanistic modelling of complex environmental systems using the GLUE methodology. J. Hydrol. 249 (1), 11–29. https://doi.org/10.1016/S0022-1694(01)00421-8.

2018 Onuchin, A.A., Buren, T.A., Balzter, H., Tsykalov, A.G., 2018. New look at understanding hydrological role of forest. https://doi.org/10.15372/SJFS20180501.

Bosch, J.M., Hewlett, J.D., 1982. A review of catchment experiments to determine the effect of vegetation changes on water yield and evapotranspiration. J. Hydrol. 55 (1–4), 3–23. https://doi.org/10.1016/0022-1694(82)90117-2.

Brown de Colstoun, E.C., Huang, C., Wang, P., Tilton, J.C., Tan, B., Phillips, J., Niemczura, S., Ling, P.-Y., Wolfe, R.E., 2017. Global man-made impervious surface (GMIS) dataset from landsat. NASA Socioecon. Data Appl. Cent. (SEDAC) Palisades NY.

Budyko, M.I., 1974. Climate and life. Academic Press, New York.

Caldwell, P., Sun, G., McNulty, S., Myers, J.M., Cohen, E., Herring, R., 2019. WaSSI Ecosyst. Serv. Model.

Caldwell, P.V., Sun, G., McNulty, S.G., Cohen, E.C., Moore Myers, J.A., 2012. Impacts of impervious cover, water withdrawals, and climate change on river flows in the conterminous US. Hydrol. Earth Syst. Sci. 16 (8), 2839–2857. https://doi.org/10.5194/hess-16-2839-2012.

Chang, X., Feng, Q., Ning, T., Xi, H., Yin, Z., 2024. Modelling and attributing growing season GPP change by improving Budyko's limitation framework in the inland river basin of Northwestern China. Agric. For. Meteorol. 355, 110139. https://doi.org/10.1016/j.agrformet.2024.110139.

Chen, J., Tang, Z., Kang, X., He, N., Li, M., 2025. Rise in wetland carbon uptake linked to increased potential evapotranspiration. Environ. Res., 121778 https://doi.org/10.1016/j.envres.2025.121778.

Chen, X., Buchberger, S.G., 2018. Exploring the relationships between warm-season precipitation, potential evaporation, and "apparent" potential evaporation at site scale. Hydrol. Earth Syst. Sci. 22 (8), 4535–4545. https://doi.org/10.5194/hess-22-4535-2018.

Dale, V.H., 1997. The relationship between land-use change and climate change. Ecol. Appl. 7 (3), 753–769. https://doi.org/10.1890/1051-0761(1997)007[0753:TRBLUC]2.0.CO;2.

Dannenberg, M.P., McCabe, G.J., Wise, E.K., Johnston, M.R., Huntzinger, D.N., Williams, A.P., 2025. Recent increases in Missouri River streamflow driven by combined effects of climate variability, land-use change, and elevated CO2. AGU Adv. 6 (2), e2024AV001432. https://doi.org/10.1029/2024AV001432.

Du, L., 2019. Carbon-water coupling of terrestrial ecosystems in response to climate change and climate variability. Doctoral dissertation. University of Oklahoma, Norman, Oklahoma, USA.

Du, L., Zeng, Y., Ma, L., Qiao, C., Wu, H., Su, Z., Bao, G., 2021. Effects of anthropogenic revegetation on the water and carbon cycles of a desert steppe ecosystem. Agric. For. Meteorol. 300, 108339. https://doi.org/10.1016/j.agrformet.2021.108339.

Duan, K., Sun, G., Sun, S., Caldwell, P.V., Cohen, E.C., McNulty, S.G., Aldridge, H.D., Zhang, Y., 2016. Divergence of ecosystem services in U.S. National forests and grasslands under a changing climate. Sci. Rep. 6 (1), 24441. https://doi.org/10.1038/srep24441.

Duan, K., Sun, G., McNulty, S.G., Caldwell, P.V., Cohen, E.C., Sun, S., Aldridge, H.D., Zhou, D., Zhang, L., Zhang, Y., 2017. Future shift of the relative roles of precipitation and temperature in controlling annual runoff in the conterminous United States. Hydrol. Earth Syst. Sci. 21 (11), 5517–5529. https://doi.org/10.5194/hess-21-5517-2017.

Duan, K., Caldwell, P.V., Sun, G., McNulty, S.G., Zhang, Y., Shuster, E., Liu, B., Bolstad, P.V., 2019. Understanding the role of regional water connectivity in mitigating climate change impacts on surface water supply stress in the United States. J. Hydrol. 570, 80–95. https://doi.org/10.1016/j.jhydrol.2019.01.011.

Duan, K., Sun, G., Liu, N., 2021. A review of research on watershed water-carbon balance evolution in a changing environment. J. Hydraul. Eng. 03, 300–309. https://doi.org/10.13243/j.cnki.slxb.20200172.

Duan, K., Wang, X., Qiu, J., 2022. A Python-based method for regional-scale extraction and visualization of hydrometeorological data. Chin. Pat. CN 114911853B (in Chinese).

Duan, K., Caldwell, P.V., Sun, G., McNulty, S.G., Qin, Y., Chen, X., Liu, N., 2022. Climate change challenges efficiency of inter-basin water transfers in alleviating water stress. Environ. Res. Lett. 17 (4), 044050. https://doi.org/10.1088/1748-9326/ac5e68.

Duan, K., Qu, S., Liu, N., Dobbs, G.R., Caldwell, P.V., Sun, G., 2023. Evolving efficiency of inter-basin water transfers in regional water stress alleviation. Resour. Conserv. Recycl. 191, 106878. https://doi.org/10.1016/j.resconrec.2023.106878.

Duan, Q., Sorooshian, S., Gupta, V.K., 1994. Optimal use of the SCE-UA global optimization method for calibrating watershed models. J. Hydrol. 158 (3–4), 265–284. https://doi.org/10.1016/0022-1694(94)90057-4.

Duarte, H.F., Kim, J.B., Sun, G., McNulty, S., Xiao, J., 2024. Climate and vegetation change impacts on future conterminous United States water yield. J. Hydrol. 639, 131472. https://doi.org/10.1016/j.jhydrol.2024.131472.

Ellison, D., Futter, M.N., Bishop, K., 2012. On the forest cover–water yield debate: from demand- to supply-side thinking. Glob. Change Biol. 18 (3), 806–820. https://doi.org/10.1111/j.1365-2486.2011.02589.x.

Farley, K.A., Jobbágy, E.G., Jackson, R.B., 2005. Effects of afforestation on water yield: a global synthesis with implications for policy. Glob. Change Biol. 11 (10), 1565–1576. https://doi.org/10.1111/j.1365-2486.2005.01011.x.

Feng, H., Wang, S., Zou, B., Yang, Z., Wang, S., Wang, W., 2023. Contribution of land use and cover change (LUCC) to the global terrestrial carbon uptake. Sci. Total Environ. 901, 165932. https://doi.org/10.1016/j.scitotenv.2023.165932.

Filoso, S., Bezerra, M.O., Weiss, K.C., Palmer, M.A., 2017. Impacts of forest restoration on water yield: a systematic review. PLoS One 12 (8), e0183210. https://doi.org/10.1371/journal.pone.0183210.

Friedl, M., Sulla-Menashe, D., 2019. MCD12Q1 MODIS/Terra + aqua land cover type Yrly. L3 Glob. 500 M. SIN grid V006. NASA EOSDIS land process. DAAC.

Gan, G., Liu, Y., Sun, G., 2021. Understanding interactions among climate, water, and vegetation with the Budyko framework. EarthSci. Rev. 212, 103451. https://doi.org/10.1016/j.earscirev.2020.103451.

Gentine, P., Green, J.K., Guérin, M., Humphrey, V., Seneviratne, S.I., Zhang, Y., Zhou, S., 2019. Coupling between the terrestrial carbon and water cycles-A review. Environ. Res. Lett. 14 (8), 083003. https://doi.org/10.1088/1748-9326/ab22d6.

Hamon, W.R., 1963. Computation of Direct Runoff Amounts from Storm Rainfall, 63. International Association of Scientific Hydrology Publication, pp. 52–62.

He, C., Ma, B., Jing, J., Xu, Y., Dou, S., 2021. Spatial-temporal variation and future changing trend of NDVI in the Pearl River Basin from 1982 to 2015. Human Centered Computing: 6th International Conference, HCC 2020, Virtual Event, December 14–15, 2020, Revised Selected Papers 6. Springer, Cham, pp. 209–219.

He, J., Yang, K., Tang, W., Lu, H., Qin, J., Chen, Y., Li, X., 2020. The first high-resolution meteorological forcing dataset for land process studies over China. Sci. Data 7 (1), 25. https://doi.org/10.1038/s41597-020-0369-y.

Hoek van Dijke, A.J., Herold, M., Mallick, K., Benedict, I., Machwitz, M., Schlerf, M., Pranindita, A., Theeuwen, J.J.E., Bastin, J.-F., Teuling, A.J., 2022. Shifts in regional water availability due to global tree restoration. Nat. Geosci. 15 (5), 363–368. https://doi.org/10.1038/s41561-022-00935-0.

Hou, H., Zhou, B., Pei, F., Hu, G., Su, Z., Zeng, Y., Zhang, H., Gao, Y., Luo, M., Li, X., 2022. Future land use/land cover change has nontrivial and potentially dominant impact on global gross primary productivity. Earths Future 10 (9), e2021EF002628. https://doi.org/10.1029/2021EF002628.

Hou, H., Li, X., Yao, Y., Hu, G., Wang, C., Chu, N., 2025. Attributing future changes in terrestrial evapotranspiration: the combined impacts of climate change, rising CO2, and land use change. Agric. For. Meteorol. 373, 110747. https://doi.org/10.1016/j.agrformet.2025.110747.

Huang, M., Piao, S., Sun, Y., Ciais, P., Cheng, L., Mao, J., Poulter, B., Shi, X., Zeng, Z., Wang, Y., 2015. Change in terrestrial ecosystem water-use efficiency over the last three decades. Glob. Change Biol. 21 (6), 2366–2378. https://doi.org/10.1111/gcb.12873.

Hutley, L.B., Beringer, J., Fatichi, S., Schymanski, S.J., Northwood, M., 2022. Gross primary productivity and water use efficiency are increasing in a high rainfall tropical savanna. Glob. Change Biol. 28 (7), 2360–2380. https://doi.org/10.1111/gcb.16012.

IPCC, 2013. Climate change 2013: the physical science basis. Contribution of Working Group I to the Fifth Assessment Report of the Intergovernmental Panel on Climate Change. Cambridge University Press, Cambridge. https://doi.org/10.1017/CBO9781107415324.

IPCC, 2023. Climate change 2023: synthesis report. contribution of working groups I, II and III to the sixth assessment report of the intergovernmental panel on climate change. IPCC, Geneva, p. 180. https://doi.org/10.59327/IPCC/AR6-9789291691647.

Jackson, R.B., Jobbágy, E.G., Avissar, R., Roy, S.B., Barrett, D.J., Cook, C.W., Farley, K.A., le Maitre, D.C., McCarl, B.A., Murray, B.C., 2005. Trading water for carbon with biological carbon sequestration. Science 310 (5756), 1944–1947. https://doi.org/10.1126/science.1119282.

Kang, T.-H., Sharma, A., 2024. A state-controlled hypothesis test for paired-watershed experiments. J. Hydrol. 640, 131664. https://doi.org/10.1016/j.jhydrol.2024.131664.

Kannenberg, S.A., Anderegg, W.R., Barnes, M.L., Dannenberg, M.P., Knapp, A.K., 2024. Dominant role of soil moisture in mediating carbon and water fluxes in dryland ecosystems. Nat. Geosci. 17 (1), 38–43. https://doi.org/10.1038/s41561-023-01351-8.

Khorchani, M., Nadal-Romero, E., Lasanta, T., Tague, C., 2022. Carbon sequestration and water yield tradeoffs following restoration of abandoned agricultural lands in Mediterranean mountains. Environ. Res. 207, 112203. https://doi.org/10.1016/j.envres.2021.112203.

Konarska, K.M., Sutton, P.C., Castellon, M., 2002. Evaluating scale dependence of ecosystem service valuation: a comparison of NOAA-AVHRR and Landsat TM datasets. Ecol. Econ. 41 (3), 491–507. https://doi.org/10.1016/S0921-8009(02)00096-4.

Lange, S., 2021. ISIMIP3b bias Adjust. Fact. Sheet InterSect. Impact Model Intercomp. Proj. (ISIMIP) Potsdam.

Lehner, B., Verdin, K., Jarvis, A., 2008. New global hydrography derived from spaceborne elevation data. Eos (Wash. DC 89 (10), 93–94. https://doi.org/10.1029/2008EO100001.

Li, C., Sun, G., Caldwell, P.V., Cohen, E., Fang, Y., Zhang, Y., Oudin, L., Sanchez, G.M., Meentemeyer, R.K., 2020. Impacts of urbanization on watershed water balances across the conterminous United States. Water Resour. Res. 56 (7), e2019WR026574. https://doi.org/10.1029/2019WR026574.

Li, C., Sun, G., Cohen, E., Zhang, Y., Xiao, J., McNulty, S.G., Meentemeyer, R.K., 2020. Modeling the impacts of urbanization on watershed-scale gross primary productivity and tradeoffs with water yield across the conterminous United States. J. Hydrol. 583, 124581. https://doi.org/10.1016/j.jhydrol.2020.124581.

Li, Q., Wei, X., Zhang, M., Liu, W., Fan, H., Zhou, G., Giles-Hansen, K., Liu, S., Wang, Y., 2017. Forest cover change and water yield in large forested watersheds: a global synthetic assessment. Ecohydrology 10 (4), e1838. https://doi.org/10.1002/eco.1838.

Li, W., Duveiller, G., Wieneke, S., Forkel, M., Gentine, P., Reichstein, M., Niu, S., Migliavacca, M., Orth, R., 2024. Regulation of the global carbon and water cycles through vegetation structural and physiological dynamics. Environ. Res. Lett. 19 (7), 073008. https://doi.org/10.1088/1748-9326/ad5858.

Li, Z., Zhou, P., Shi, X., Li, Y., 2021. Forest effects on runoff under climate change in the Upper Dongjiang River basin: insights from annual to intra-annual scales. Environ. Res. Lett. 16 (1), 014032. https://doi.org/10.1088/1748-9326/abd066.

Li, Z., Jiang, W., Hou, P., Peng, K., Deng, Y., Wang, X., 2023. Changes in the ecosystem service importance of the seven major river basins in China during the implementation of the Millennium Development Goals (2000–2015) and Sustainable Development Goals. J. Clean. Prod. 433, 139787. https://doi.org/10.1016/j.jclepro.2023.139787.

Liao, W., Liu, X., Xu, X., Chen, G., Liang, X., Zhang, H., Li, X., 2020. Projections of land use changes under the plant functional type classification in different SSP-RCP scenarios in China. Sci. Bull. 65 (22), 1935–1947. https://doi.org/10.1016/j.scib.2020.07.014.

Liu, J., Zhou, Z., Yan, Z., Gong, J., Jia, Y., Xu, C.-Y., Wang, H., 2019. A new approach to separating the impacts of climate change and multiple human activities on water cycle processes based on a distributed hydrological model. J. Hydrol. 578, 124096. https://doi.org/10.1016/j.jhydrol.2019.124096.

Liu, N., Shaikh, M.A., Kala, J., Harper, R.J., Dell, B., Liu, S., Sun, G., 2018. Parallelization of a distributed ecohydrological model. Environ. Model. Softw. 101, 51–63. https://doi.org/10.1016/j.envsoft.2017.11.033.

Liu, Y., Xiao, J., Ju, W., Xu, K., Zhou, Y., Zhao, Y., 2016. Recent trends in vegetation greenness in China significantly altered annual evapotranspiration and water yield. Environ. Res. Lett. 11 (9), 094010. https://doi.org/10.1088/1748-9326/11/9/094010.

Liu, Z., Yu, X., Liu, C., Zou, Z., Peng, C., Li, P., Tang, J., Liu, H., Zhu, Y., Huang, C., 2025. Integrating territorial pattern changes into the relationship between carbon sequestration and water yield in the Yangtze River Basin, China. Carbon Balance Manag 20 (1). https://doi.org/10.1186/s13021-024-00289-7.

Lørup, J.K., Refsgaard, J.C., Mazvimavi, D., 1998. Assessing the effect of land use change on catchment runoff by combined use of statistical tests and hydrological modelling: case studies from Zimbabwe. J. Hydrol. 205 (3–4), 147–163. https://doi.org/10.1016/S0168-1176(97)00311-9.

Lu, Z., Zou, S., Qin, Z., Yang, Y., Xiao, H., Wei, Y., Zhang, K., Xie, J., 2015. Hydrologic responses to land use change in the Loess Plateau: case study in the Upper Fenhe River Watershed. Adv. Meteorol. 2015, 1–10. https://doi.org/10.1155/2015/676030.

Luan, J., Zhang, Y., Ma, N., Tian, J., Li, X., Liu, D., 2021. Evaluating the uncertainty of eight approaches for separating the impacts of climate change and human activities on streamflow. J. Hydrol. 601, 126605. https://doi.org/10.1016/j.jhydrol.2021.126605.

Onuchin, A., Burenina, T., Shvidenko, A., Prysov, D., Musokhranova, A., 2021. Zonal aspects of the influence of forest cover change on runoff in northern river basins of Central Siberia. For. Ecosyst. 8 (1), 45. https://doi.org/10.1186/s40663-021-00316-w.

Pilla, R.M., Griffiths, N.A., Gu, L., Kao, S.C., McManamay, R., Ricciuto, D.M., Shi, X., 2022. Anthropogenically driven climate and landscape change effects on inland water carbon dynamics: what have we learned and where are we going? Glob. Change Biol. 28 (19), 5601–5629. https://doi.org/10.1111/gcb.16324.

Qi, Z., Cai, Y., Lin, J., Xie, Y., Yao, L., Zhang, P., Wang, Y., Guo, H., 2023. Coupled high-resolution GCM downscaling framework for projecting dynamics and drivers of ecosystem services in Pearl River Basin, China. Ecol. Indic. 154, 110770. https://doi.org/10.1016/j.ecolind.2023.110770.

Qi, Z., Sun, L., Cai, Y., Xie, Y., Yao, L., Li, B., Ye, Y., 2024a. Spatial-temporal dynamics of population exposure to compound extreme heat-precipitation events under multiple scenarios for Pearl River Basin, China. Clim. Serv. 34, 100477. https://doi.org/10.1016/j.cliser.2024.100477.

Qiu, J., Liu, B., Yang, F., Wang, X., He, X., 2022. Quantitative stress test of compound coastal-fluvial floods in China's Pearl River Delta. Earths Future 10 (5), e2021EF002638. https://doi.org/10.1029/2021EF002638.

Qiu, J., Ravela, S., Emanuel, K., 2025. From decades to years: rising seas and cyclones amplify Bangladesh's storm-tide hazards in a warming climate. One Earth 8 (4). https://doi.org/10.1016/j.oneear.2025.101273.

Quan, Q., Tian, D., Luo, Y., Zhang, F., Crowther, T.W., Zhu, K., Niu, S., 2019. Water scaling of ecosystem carbon cycle feedback to climate warming. Sci. Adv. 5 (8), eaav1131. https://doi.org/10.1126/sciadv.aav1131.

Rawat, A., Kumar, D., Khati, B.S., 2024. A review on climate change impacts, models, and its consequences on different sectors: a systematic approach. J. Water Clim. Change 15 (1), 104–126. https://doi.org/10.2166/wcc.2023.536.

Refsgaard, J.C., van der Sluijs, J.P., Brown, J., van der Keur, P., 2006. A framework for dealing with uncertainty due to model structure error. Adv. Water Resour. 29 (11), 1586–1597. https://doi.org/10.1016/j.advwatres.2005.11.013.

Roderick, M.L., Farquhar, G.D., 2011. A simple framework for relating variations in runoff to variations in climatic conditions and catchment properties. Water Resour. Res. 47 (12). https://doi.org/10.1029/2010WR009826.

Seto, K.C., Güneralp, B., Hutyra, L.R., 2012. Global forecasts of urban expansion to 2030 and direct impacts on biodiversity and carbon pools. Proc. Natl. Acad. Sci. U. S. A. 109 (40), 16083–16088. https://doi.org/10.1073/pnas.1211658109.

Shi, X.Z., Yu, D.S., Xu, S.X., Warner, E.D., Wang, H.J., Sun, W.X., Zhao, Y.C., Gong, Z.T., 2010. Cross-reference for relating genetic soil classification of China with WRB at different scales. Geoderma 155 (3–4), 344–350. https://doi.org/10.1016/j.geoderma.2009.12.017.

Shrestha, R., Tachikawa, Y., Takara, K., 2006. Input data resolution analysis for distributed hydrological modeling. J. Hydrol. 319 (1), 36–50. https://doi.org/10.1016/j.jhydrol.2005.04.025.

Sitch, S., O'Sullivan, M., Robertson, E., Friedlingstein, P., Albergel, C., Anthoni, P., Arneth, A., Arora, V.K., Bastos, A., Bastrikov, V., Bellouin, N., Canadell, J.G., Chini, L., Ciais, P., Falk, S., Harris, I., Hurtt, G., Ito, A., Jain, A.K., et al., 2024. Trends and drivers of terrestrial sources and sinks of carbon dioxide: an overview of the TRENDY project. Glob. Biogeochem. Cycles 38 (7), e2024GB008102. https://doi.org/10.1029/2024GB008102.

Souza da Silva, L., Ferraz, L.L., Farias de Sousa, L., Mota de Jesus, R., Silva Santos, C.A., Rocha, F.A., 2023. Assessment of changes in land use and occupation on the hydrological regime of a basin in the west of Bahia. J. S. Am. Earth Sci. 123, 104218. https://doi.org/10.1016/j.jsames.2023.104218.

Sun, G., Caldwell, P., Noormets, A., McNulty, S.G., Cohen, E., Moore Myers, J., Domec, J.-C., Treasure, E., Mu, Q., Xiao, J., John, R., Chen, J., 2011. Upscaling key ecosystem functions across the conterminous United States by a water-centric ecosystem model. J. Geophys. Res. 116, G00J05. https://doi.org/10.1029/2010JG001573.

Sun, S., Sun, G., Caldwell, P., McNulty, S.G., Cohen, E., Xiao, J., Zhang, Y., 2015. Drought impacts on ecosystem functions of the U.S. National Forests and Grasslands: part I evaluation of a water and carbon balance model. For. Ecol. Manag. 353, 260–268. https://doi.org/10.1016/j.foreco.2015.03.054.

Sun, W., Zhou, S., Yu, B., Zhang, Y., Keenan, T., Fu, B., 2025. Soil moisture-atmosphere interactions drive terrestrial carbon-water trade-offs. Commun. Earth Environ. 6 (1), 169. https://doi.org/10.1038/s43247-025-02145-z.

Tang, J., Wang, W., Cheng, H., Jin, H., Zhao, T., Xie, Y., 2024. Changes in runoff and sediment discharge along with their driving factors in the Pearl River basin from 1961 to 2018. Int. J. Sediment Res. 39 (3), 386–400. https://doi.org/10.1016/j.ijsrc.2024.02.003.

Tang, L.-L., Cai, X.-B., Gong, W.-S., Lu, J.-Z., Chen, X.-L., Lei, Q., Yu, G.-L., 2018. Increased vegetation greenness aggravates water conflicts during lasting and intensifying drought in the Poyang Lake Watershed, China. Forests 9 (1), 24. https://doi.org/10.3390/f9010024.

Teuling, A.J., De Badts, E.A., Jansen, F.A., Fuchs, R., Buitink, J., Hoek van Dijke, A.J., Sterling, S.M., 2019. Climate change, reforestation/afforestation, and urbanization impacts on evapotranspiration and streamflow in Europe. Hydrol. Earth Syst. Sci. 23 (9), 3631–3652. https://doi.org/10.5194/hess-23-3631-2019.

Tharammal, T., Bala, G., Devaraju, N., Nemani, R., 2019. A review of the major drivers of the terrestrial carbon uptake: model-based assessments, consensus, and uncertainties. Environ. Res. Lett. 14 (9), 093005. https://doi.org/10.1088/1748-9326/ab3012.

Tian, Q., Yang, S., 2017. Regional climatic response to global warming: Trends in temperature and precipitation in the Yellow, Yangtze and Pearl River basins since the 1950s. Quat. Int. 440, 1–11. https://doi.org/10.1016/j.quaint.2016.02.066.

Uribe, M.D.R., Coe, M.T., Castanho, A.D., Macedo, M.N., Valle, D., Brando, P.M., 2023. Net loss of biomass predicted for tropical biomes in a changing climate. Nat. Clim. Change 13 (3), 274–281. https://doi.org/10.1038/s41558-023-01600-z.

Vereecken, H., Amelung, W., Bauke, S.L., Bogena, H., Brüggemann, N., Montzka, C., et al., 2022. Soil hydrology in the Earth system. Nat. Rev. Earth Environ. 3 (9), 573–587. https://doi.org/10.1038/s43017-022-00324-6.

Wang, H., Duan, K., Liu, B., Chen, X., 2021. Assessing the large-scale plant–water relations in the humid, subtropical Pearl River basin of China. Hydrol. Earth Syst. Sci. 25 (9), 4741–4758. https://doi.org/10.5194/hess-25-4741-2021.

Wang, X., Duan, K., Wei, L., 2022. Simulation of water and carbon coupling of the Pearl River basin based on the WaSSI model. Chin. J. Appl. Ecol. 33 (05), 1377–1386. https://doi.org/10.13287/j.1001-9332.202205.022.

Wang, Y.P., Zhang, L., Liang, X., Yuan, W., 2024. Coupled models of water and carbon cycles from leaf to global: a retrospective and a prospective. Agric. For. Meteor. 358, 110229. https://doi.org/10.1016/j.scitotenv.2019.134064.

Wei, X., Zhang, M., 2010. Quantifying streamflow change caused by forest disturbance at a large spatial scale: a single watershed study. Water Resour. Res. 46 (12). https://doi.org/10.1029/2010WR009250.

Wei, X., Liu, W., Zhou, P., 2013. Quantifying the relative contributions of forest change and climatic variability to hydrology in large watersheds: a critical review of research methods. Water 5 (2), 728–746. https://doi.org/10.3390/w5020728.

Wei, X., Li, Q., Zhang, M., Giles-Hansen, K., Liu, W., Fan, H., Wang, Y., Zhou, G., Piao, S., Liu, S., 2018. Vegetation cover—another dominant factor in determining global water resources in forested regions. Glob. Change Biol. 24 (2), 786–795. https://doi.org/10.1111/gcb.13983.

Whitney, K.M., Vivoni, E.R., Bohn, T.J., Mascaro, G., Wang, Z., Xiao, M., Mahmoud, M.I., Cullom, C., White, D.D., 2023. Spatial attribution of declining Colorado River streamflow under future warming. J. Hydrol. 617, 129125. https://doi.org/10.1016/j.jhydrol.2023.129125.

Whittaker, G., Confesor, R., Di Luzio, M., Arnold, J.G., 2010. Detection of overparameterization and overfitting in an automatic calibration of SWAT. Trans. ASABE 53 (5), 1487–1499. https://doi.org/10.13031/2013.34909.

te Wierik, S.A., Cammeraat, E.L., Gupta, J., Artzy-Randrup, Y.A., 2021. Reviewing the impact of land use and land-use change on moisture recycling and precipitation patterns. Water Resour. Res. 57 (7), e2020WR029234. https://doi.org/10.1029/2020WR029234.

Woldesenbet, T.A., Elagib, N.A., Ribbe, L., Heinrich, J., 2017. Hydrological responses to land use/cover changes in the source region of the Upper Blue Nile Basin, Ethiopia. Sci. Total Environ. 575, 724–741. https://doi.org/10.1016/j.scitotenv.2016.09.124.

Wu, B.W., Zhang, Y.Y., Wang, Y., Lin, X.B., Wu, Y.F., Wang, J.W., Wu, S.D., He, Y.M., 2024. Urbanization promotes carbon storage or not? The evidence during the rapid process of China. J. Environ. Manag. 359, 121061. https://doi.org/10.1016/j.jenvman.2024.121061.

Wu, J., Miao, C., Zhang, X., Yang, T., Duan, Q., 2017. Detecting the quantitative hydrological response to changes in climate and human activities. Sci. Total Environ. 586, 328–337. https://doi.org/10.1016/j.scitotenv.2017.02.010.

Wu, X., Shi, W., Guo, B., Tao, F., 2020. Large spatial variations in the distributions of and factors affecting forest water retention capacity in China. Ecol. Indic. 113, 106152. https://doi.org/10.1016/j.ecolind.2020.106152.

Xiao, B., Bai, X., Zhao, C., Tan, Q., Li, Y., Luo, G., Wu, L., Chen, F., Li, C., Ran, C., Luo, X., Xi, H., Chen, H., Zhang, S., Liu, M., Gong, S., Xiong, L., Song, F., Du, C., 2023. Responses of carbon and water use efficiencies to climate and land use changes in China's karst areas. J. Hydrol. 617, 128968. https://doi.org/10.1016/j.jhydrol.2022.128968.

Xiao, J., Xie, B., Zhou, K., Li, J., Xie, J., Liang, C., 2022. Contributions of climate change, vegetation growth, and elevated atmospheric CO_2 concentration to variation in water use efficiency in subtropical China. Remote Sens 14 (17), 4296. https://doi.org/10.3390/rs14174296.

Xu, X., Jiao, F., Liu, H., Gong, H., Zou, C., Lin, N., Xue, P., Zhang, M., Wang, K., 2022. Persistence of increasing vegetation gross primary production under the interactions of climate change and land use changes in Northwest China. Sci. Total Environ. 834, 155086. https://doi.org/10.1016/j.scitotenv.2022.155086.

Xu, X., Liu, J., Jiao, F., Zhang, K., Ye, X., Gong, H., Lin, N., Zou, C., 2023. Ecological engineering induced carbon sinks shifting from decreasing to increasing during 1981–2019 in China. Sci. Total Environ. 864, 161037. https://doi.org/10.1016/j.scitotenv.2022.161037.

Xue, B., A, Y., Wang, G., Helman, D., Sun, G., Tao, S., Liu, T., Yan, D., Zhao, T., Zhang, H., Chen, L., Sun, W., Xiao, J., 2022. Divergent hydrological responses to forest expansion in dry and wet basins of China: Implications for future afforestation planning. e2021WR031856 Water Resour. Res. 58 (5). https://doi.org/10.1029/2021WR031856.

Yan, D., Werners, S.E., Ludwig, F., Huang, H.Q., 2015. Hydrological response to climate change: the Pearl River, China under different RCP scenarios. J. Hydrol. Reg. Stud. 4, 228–245. https://doi.org/10.1016/j.ejrh.2015.06.006.
Yang, K., He, J., Tang, W., Qin, J., Cheng, C.C., 2010. On downward shortwave and longwave radiations over high altitude regions: Observation and modeling in the Tibetan Plateau. Agric. For. Meteorol. 150 (1), 38–46. https://doi.org/10.1016/j.agrformet.2009.08.004.
Yang, K., He, J., Tang, W., Lu, H., Qin, J., Chen, Y., Li, X., 2020. China meteorological forcing dataset (1979–2018) [Dataset. Natl. Tibet. Plateau / Third Pole Environ. Data Cent. https://doi.org/10.11888/AtmosphericPhysics.tpe.249369.file.
Yang, L., Feng, Q., Yin, Z., Wen, X., Si, J., Li, C., Deo, R.C., 2017. Identifying separate impacts of climate and land use/cover change on hydrological processes in upper stream of Heihe River, Northwest China. Hydrol. Process. 31 (5), 1100–1112. https://doi.org/10.1002/hyp.11098.
Yang, L., Zhao, G., Tian, P., Mu, X., Tian, X., Feng, J., Bai, Y., 2022. Runoff changes in the major river basins of China and their responses to potential driving forces. J. Hydrol. 607, 127536. https://doi.org/10.1016/j.jhydrol.2022.127536.
Yang, Q., Qi, Z., Ye, Y., Xie, Y., Zhang, P., Zhang, C., Cai, Y., 2025. Projected increase in soil erosion risk in the karst landscape of the Pearl River Basin under high carbon emission scenarios. Catena 256, 109065. https://doi.org/10.1016/j.catena.2025.109065.
Yang, R., Yuan, H., Du, R., Zhou, L., Wu, J., Gao, L., Mao, T., 2025. Temperature–VPD–evapotranspiration interactions modulated asynchronous dynamics of vegetation photosynthesis and net ecosystem production in Eurasia. Ecol. Indic. 174, 113445. https://doi.org/10.1016/j.ecolind.2025.113445.
Yang, S., Zhao, B., Yang, D., Wang, T., Yang, Y., Ma, T., Santisirisomboon, J., 2023. Future changes in water resources, floods and droughts under the joint impact of climate and land-use changes in the Chao Phraya basin, Thailand. J. Hydrol. 620, 129454. https://doi.org/10.1016/j.jhydrol.2023.129454.
Yang, W., Long, D., Bai, P., 2019. Impacts of future land cover and climate changes on runoff in the mostly afforested river basin in North China. J. Hydrol. 570, 201–219. https://doi.org/10.1016/j.jhydrol.2018.12.055.
Yang, Y., Li, M., Feng, X., Yan, H., Su, M., Wu, M., 2021. Spatiotemporal variation of essential ecosystem services and their trade-off/synergy along with rapid urbanization in the Lower Pearl River Basin, China. Ecol. Indic. 133, 108439. https://doi.org/10.1016/j.ecolind.2021.108439.
Yen, H., Wang, X., Fontane, D.G., Harmel, R.D., Arabi, M., 2014. A framework for propagation of uncertainty contributed by parameterization, input data, model structure, and calibration/validation data in watershed modeling. Environ. Model. Softw. 54, 211–221. https://doi.org/10.1016/j.envsoft.2014.01.004.
Yin, S., Gao, G., Huang, A., Li, D., Ran, L., Nawaz, M., Xu, Y.J., Fu, B., 2023. Streamflow and sediment load changes from China's large rivers: quantitative contributions of climate and human activity factors. Sci. Total Environ. 876, 162758. https://doi.org/10.1016/j.scitotenv.2023.162758.
Yonaba, R., Mounirou, L.A., Tazen, F., Koïta, M., Biaou, A.C., Zouré, C.O., Queloz, P., Karambiri, H., Yacouba, H., 2023. Future climate or land use? Attribution of changes in surface runoff in a typical Sahelian landscape. C. R. Geosci. 355 (S1), 411–438. https://doi.org/10.5802/crgeos.179.
Yuan, H., Dai, Y., Xiao, Z., Ji, D., Shangguan, W., 2011. Reprocessing the MODIS leaf area index products for land surface and climate modelling. Remote Sens. Environ. 115 (5), 1171–1187. https://doi.org/10.1016/j.rse.2011.01.001.
Zeng, Z., Wu, W., Li, Y., Huang, C., Zhang, X., Pẽnuelas, J., Zhang, Y., Gentine, P., Li, Z., Wang, X., Huang, H., Ren, X., Ge, Q., 2023. Increasing meteorological drought under climate change reduces terrestrial ecosystem productivity and carbon storage. One Earth 6, 1326–1339. https://doi.org/10.1016/j.oneear.2023.09.007.
Zhang, B., Tian, L., He, C., He, X., 2023. Response of erosive precipitation to vegetation restoration and its effect on soil and water conservation over China's Loess Plateau. Water Resour. Res. 59 (1), e2022WR033382. https://doi.org/10.1029/2022WR033382.
Zhang, J., Zhang, Y., Sun, G., Song, C., Dannenberg, M.P., Li, J., Liu, N., Zhang, K., Zhang, Q., Hao, L., 2021. Vegetation greening weakened the capacity of water supply to China's South-to-North Water Diversion Project. Hydrol. Earth Syst. Sci. 25, 5623–5640. https://doi.org/10.5194/hess-25-5623-2021.
Zhang, J., Zhang, Y., Sun, G., Song, C., Li, J., Hao, L., Liu, N., 2022. Climate variability masked greening effects on water yield in the Yangtze River Basin during 2001–2018. Water Resour. Res. 58 (1), e2021WR030382. https://doi.org/10.1029/2021WR030382.
Zhang, L., Duan, K., Zhang, Y., Sun, G., Liang, X., 2025. Impacts of anthropogenic emission change scenarios on US water and carbon balances at national and state scales in a changing climate. Earth'S. Future 13 (4), e2024EF004853. https://doi.org/10.1029/2024EF004853.
Zhang, X., Chen, Y., Zhang, Q., Xia, Z., Hao, H., Xia, Q., 2023. Potential evapotranspiration determines changes in the carbon sequestration capacity of forest and grass ecosystems in Xinjiang, Northwest China. Glob. Ecol. Conserv. 48, e02737. https://doi.org/10.1016/j.gecco.2023.e02737.
Zhang, Y., Gan, J., 2025. Spatiotemporal dynamics of future hydrology in the Pearl River Basin: Controls of climate change and land surface. J. Hydrol. Reg. Stud. 58, 102239. https://doi.org/10.1016/j.ejrh.2025.102239.
Zhang, Y., Hao, L., 2025. Direct and indirect effects of large-scale forest restoration on water yield in China's Large River Basins. Remote Sens 17 (9), 1581. https://doi.org/10.3390/rs17091581.
Zhao, F., Wu, Y., Yin, X., Alexandrov, G., Qiu, L., 2022. Toward sustainable revegetation in the loess plateau using coupled water and carbon management. Engineering 15, 143–153. https://doi.org/10.1016/j.eng.2020.12.017.
Zheng, Y., Zhang, L., Xiao, J., Yuan, W., Yan, M., Li, T., Zhang, Z., 2018. Sources of uncertainty in gross primary productivity simulated by light use efficiency models: model structure, parameters, input data, and spatial resolution. Agric. For. Meteorol. 263, 242–257. https://doi.org/10.1016/j.agrformet.2018.08.003.
Zhou, G., Wei, X., Luo, Y., Zhang, M., Li, Y., Qiao, Y., Liu, H., Wang, C., 2010. Forest recovery and river discharge at the regional scale of Guangdong Province, China. Water Resour. Res. 46 (9). https://doi.org/10.1029/2009WR008829.
Zhou, S., Yu, B., Huang, Y., Wang, G., 2014. The effect of vapor pressure deficit on water use efficiency at the subdaily time scale. Geophys. Res. Lett. 41 (14), 5005–5013. https://doi.org/10.1002/2014GL060741.
Zongxing, L., Qi, F., Wei, L., Tingting, W., Yan, G., Yamin, W., Aifang, C., Jianguo, L., Li, L., 2014. Spatial and temporal trend of potential evapotranspiration and related driving forces in Southwestern China, during 1961–2009. Quat. Int. 336, 127–144. https://doi.org/10.1016/j.quaint.2013.12.045.